J. Fluid Mech. (2008), *vol.* 605, *pp.* 79–113.
doi:10.1017/S0022112008001365 Printed in the United Kingdom

Experimental studies of the viscous boundary layer properties in turbulent Rayleigh–Bénard convection

CHAO SUN, YIN-HAR CHEUNG AND KE-QING XIA

Department of Physics, The Chinese University of Hong Kong, Shatin, Hong Kong, China

(Received 17 October 2007 and in revised form 25 February 2008)

We report high-resolution measurements of the properties of the velocity boundary layer in turbulent thermal convection using the particle image velocimetry (PIV) technique and measurements of the temperature profiles and the thermal boundary layer. Both velocity and temperature measurements were made near the lower conducting plate of a rectangular convection cell using water as the convecting fluid, with the Rayleigh number Ra varying from 10^9 to 10^{10} and the Prandtl number Pr fixed at 4.3. From the measured profiles of the horizontal velocity we obtain the viscous boundary layer thickness δ_v. It is found that δ_v follows the classical Blasius-like laminar boundary layer in the present range of Ra, and it scales with the Reynolds number Re as $\delta_v/H = 0.64Re^{-0.50\pm0.03}$ (where H is the cell height). While the measured viscous shear stress and Reynolds shear stress show that the boundary layer is laminar for $Ra < 2.0 \times 10^{10}$, two independent extrapolations, one based on velocity measurements and the other on velocity and temperature measurements, both indicate that the boundary layer will become turbulent at $Ra \sim 10^{13}$. Just above the thermal boundary layer but within the mixing zone, the measured temperature r.m.s. profiles $\sigma_T(z)$ are found to follow either a power law or a logarithmic behaviour. The power-law fitting may be slightly favoured and its exponent is found to depend on Ra and varies from -0.6 to -0.77, which is much larger than the classical value of $-1/3$. In the same region, the measured profiles of the r.m.s. vertical velocity $\sigma_w(z)$ exhibit a much smaller scaling range and are also consistent with either a power-law or a logarithmic behaviour. The Reynolds number dependence of several wall quantities is also measured directly. These are the wall shear stress $\tau_w \sim Re^{1.55}$, the viscous sublayer $\delta_w \sim Re^{-0.91}$, the friction velocity $u_\tau \sim Re^{0.80}$, and the skin-friction coefficient $c_f \sim Re^{-0.34}$. All of these scaling properties are very close to those predicted for a classical Blasius-type laminar boundary layer, except that of c_f. Similar to classical shear flows, a viscous sublayer is also found to exist in the present system despite the presence of a nested thermal boundary layer. However, velocity profiles normalized by wall units exhibit no obvious logarithmic region, which is likely to be a result of the very limited distance between the edge of the viscous sublayer and the position of the maximum velocity. Compared to traditional shear flows, the peak position of the wall-unit-normalized r.m.s. profiles is found to be closer to the plate (at $z^+ = z/\delta_w \simeq 5$). Our overall conclusion is that a Blasius-type laminar boundary condition is a good approximation for the velocity boundary layer in turbulent thermal convection for the present range of Rayleigh number and Prandtl number.

1. Introduction

1.1. *General*

Turbulent Rayleigh–Bénard convection has attracted much interest during the past decade, partly due to its relevance to astrophysical and geophysical phenomena such as solar and mantle convections and partly because it is an ideal system to study thermal turbulence in a closed box (Castaing *et al.* 1989; Siggia 1994; Kadanoff 2001). In turbulent convection, the flow is initiated and maintained by the buoyancy force produced by an applied constant temperature difference across the height of the convection cell. The dynamics of the flow is characterized by the geometry of the cell and two control parameters, namely the Rayleigh number Ra and the Prandtl number Pr. The Rayleigh number measures the ratio between the buoyancy force driving the flow and the thermal and viscous dissipative forces that damp it, and is defined as $Ra = \alpha g \triangle T H^3/\nu\kappa$. Here α is the thermal expansion coefficient, g the gravitational acceleration, $\triangle T$ the temperature difference between the bottom and the top plates, H the height of the fluid layer between the plates, and ν and κ are the kinematic viscosity and the thermal diffusivity of the convecting fluid respectively. The Prandtl number is defined as $Pr = \nu/\kappa$, and it measures the relative strengths of two molecular processes, i.e. diffusion of momentum and heat and sets the relative size of the thermal and viscous length scales in the system.

A central issue in the study of turbulent thermal convection is to understand how turbulent flows transport heat across the fluid layer. A measure of heat transfer enhancement by convection is the Nusselt number $Nu = QH/\lambda_f \triangle T$, where Q is the heat flux density across a fluid layer of thermal conductivity λ_f. To determine the Ra- and Pr-dependence of Nu, many experimental (Castaing *et al.* 1989; Takeshita *et al.* 1996; Cioni, Ciliberto & Sommeria 1997; Du & Tong 1998; Glazier *et al.* 1999; Xia & Qiu 1999; Ashkenazi & Steinberg 1999; Niemela *et al.* 2000; Ahlers & Xu 2001; Chavanne *et al.* 2001; Xia, Lam & Zhou 2002; Niemela & Sreenivasan 2003; Shang *et al.* 2003) and numerical (Kerr 1996; Kenjereš & Hanjalić 2002; Verzicco & Camussi 2003; Breuer *et al.* 2004; Amati *et al.* 2005) studies have been done in various fluids and cell geometries. On the theoretical side, several models have been proposed (Kraichnan 1962; Castaing *et al.* 1989; Shraiman & Siggia 1990; Grossmann & Lohse 2000, 2001 2004; Dubrulle 2001). Through these studies, it is now possible to make detailed and high-precision comparisons between theory and experiment. An example is the excellent agreement between Nu measured by Ahlers & Xu (2001) and by Xia *et al.* (2002) and the model prediction by Grossmann & Lohse (2001) over a wide range of Ra and Pr. Recently, the issue of aspect ratio Γ (lateral dimension of the fluid layer over its height) has been raised (Niemela & Sreenivasan 2003; Grossmann & Lohse 2003; Ching & Tam 2006) and measurements of Nu over a varying range of Γ have been made (Nikolaenko *et al.* 2005; Funfschilling *et al.* 2005; Sun *et al.* 2005*a*; Niemela & Sreenivasan 2006).

1.2. *The thermal and viscous boundary layers in turbulent thermal convection*

At sufficiently high values of Ra, a large-scale circulation (LSC) is formed across the height of the convection cell (Krishnamurti & Howard 1981). This circulation, also known as the 'wind' in turbulent convection, has been studied extensively in recent years, experimentally, theoretically and numerically (see, for example, Xi, Zhou & Xia 2006, which contains a large compilation of relevant references). As it sweeps across the conducting plates, the LSC stabilizes the thermal boundary layer below/above via its shear, which also creates a viscous boundary layer. Except for cases of very small

Pr such as convection in liquid metals, the viscous layer is usually thicker than the thermal layer. It has long been recognized that thermal and viscous boundary layers near the upper and lower surfaces play an important role in determining the heat flux and temperature and velocity statistics (Thomas & Townsend 1957; Priestley 1959; Townsend 1959). A manifestation of this is the limitation the thickness of the thermal boundary layer imposes on the amount of heat that can be transported across a Rayleigh–Bénard convection cell, as heat is transferred by conduction within the thermal boundary layer. However, the thermal boundary layer is not isolated but modified and stabilized by viscous shear of the LSC. This viscous shear also produces a velocity boundary layer that is dynamically coupled to the thermal one.

Characterization of both boundary layers and their interplay is thus an important part of the study of turbulent convection. By assuming that the velocity boundary layer in turbulent convection is similar to those in shear flows, logarithmic corrections to scaling have been introduced in theoretical models (Shraiman & Siggia 1990; Siggia 1994; Dubrulle 2001). Taking a different approach, Grossmann & Lohse (2000, 2001) (referred to as GL) have put forward a theory that separates the viscous and thermal dissipation rates into boundary layer and bulk contributions. By considering the relative strengths of the boundary layer and bulk parts of the two dissipation rates, GL obtained various flow regimes in the (*Ra, Pr*) phase plane. The model has successfully explained some observed scaling laws in the system (GL 2000, 2001, 2004). An important assumption of the GL model is that the velocity (or viscous) boundary layer behaves as a classical Blasius-type laminar layer. A defining feature of the Blasius boundary layer is that its thickness δ_v scales as $1/\sqrt{Re}$. In turbulent thermal convection, this result has so far not been observed experimentally in the horizontal thermal conducting boundary, except near the vertical sidewall (Qiu & Xia 1998*a*) where the boundary is thermally insulating.

1.3. *Previous thermal boundary layer measurements in turbulent thermal convection*

Compared to those devoted to the bulk fluid of the system, experimental studies of boundary layer properties in turbulent thermal convection are rather limited. For the thermal boundary layer, Tilgner, Belmonte & Libchaber (1993) measured temperature profiles at a fixed *Ra* (1.1×10^9) using water as the working fluid and obtained the thermal boundary layer thickness. Belmonte, Tilgner & Libchaber (1993) also carried out temperature boundary layer measurements using gas at room temperature for *Ra* from 5×10^5 to 1×10^{11}. They found that the *Ra*-dependence of the thermal boundary layer thickness is close to $Ra^{-2/7}$ for $Ra > 2 \times 10^7$. Lui & Xia (1998) made a systematic study of the spatial structures of the thermal boundary layer at various positions over the bottom plate of a cylindrical convection cell with *Ra* varied from 2×10^8 to 2×10^{10}, also using water as convecting fluid. Their results show that the thermal boundary thickness at various positions of the plate is strongly modified by the large-scale circulation, and that the scaling exponent of the boundary layer with *Ra* is position-dependent. Their results also suggest that the boundary layer thickness will eventually become uniform across the plate at very high *Ra*.

In a subsequent study, Wang & Xia (2003) measured the spatial structure of the thermal boundary layer and its scaling dependence on *Ra* in a cubic cell filled with water, with *Ra* varying from 10^8 to 10^{10}. They also studied the statistical properties of the temperature field both near the boundary and in the bulk. Similar to the case in a cylindrical cell, Wang & Xia (2003) found that the thickness of the thermal boundary layer in the cubic cell also depends on the horizontal position across the plate. In

addition, they found that the profiles of the temperature r.m.s. measured for different values of Ra can be scaled to collapse on a single curve, in contrast to the finding that the shape of the scaled mean temperature profiles depends on Ra in both cylindrical (Lui & Xia 1998) and cubic cells (Wang & Xia 2003). In a theoretical study, Ching (1997) found a connection between the shape of the temperature profile and the heat flux.

How the temperature and velocity r.m.s. profiles scale with distance near the horizontal plate is also an issue of importance, because their scaling properties may be used to differentiate the various theoretical models that make the same predictions for global quantities such as the Nusselt number but have different assumptions for the fluctuating velocity and temperature in the boundary layer region (Adrian 1996). However, experimentally the situation is far from settled. In an experiment using water as working fluid, Fernandes & Adrian (2002) reported observing logarithmic profiles for both the temperature r.m.s. σ_T and the vertical velocity r.m.s. σ_w. On the other hand, in a recent experiment using air as convecting fluid and with Ra reaching 10^{12}, Puits *et al.* (2007) found that the profiles of σ_T follow a power-law behaviour with an exponent that depends on both Ra and Γ.

1.4. *Previous viscous boundary layer measurements in turbulent thermal convection*

The viscous boundary layer is notoriously difficult to measure in thermal turbulence, as large temperature fluctuations make conventional velocimetry techniques such as laser Doppler velocimetry (LDV) ineffective in the boundary layer region. This is because temperature fluctuations cause fluctuations in the refractive index of the fluid that in turn make it difficult to steadily focus two laser beams to cross each other in the fluid, a prerequisite for LDV. Partly because of the technical difficulties, experimental studies on velocity boundary layers are rather limited. Tilgner *et al.* (1993), using a electrochemical labelling method, measured the velocity profile near the top plate of a cubic cell filled with water and then determined the boundary layer thickness from the measured profile. Because of the cumbersome procedure of the method, the velocity measurements were conducted only at a single value of Ra (1.1×10^9). In a later study, Belmonte, Tilgner & Libchaber (1993, 1994) developed an indirect method — the correspondence between the peak position of the cutoff frequency (highest excitation frequency above noise) profile of the temperature power spectrum and the peak position of the velocity – to infer the viscous boundary layer thickness in gaseous convection. This method has subsequently been used to infer the viscous layer in thermal convection in mercury (Naert, Segawa & Sano, 1997). In a more systematic test of this method in water Xia & Zhou (2000) found that the obtained boundary layer thickness agrees with that from direct light scattering measurements (see below). But a justification for this method is not borne out in the same study, which casts doubt over the validity of extending it to other fluids with different Pr.

Using a novel light-scattering technique (Xia, Xin & Tong 1995) that avoids the crossing of two laser beams required in LDV, Xin, Xia & Tong (1996) made direct velocity boundary layer measurements near the bottom plate in a cylindrical cell filled with water. Over the range of Ra from 10^8 to 10^{10}, they determined that the viscous boundary layer thickness has a scaling relation of $\delta_v \sim Ra^{-0.16\pm0.02}$. In a later study using the same technique, Xin & Xia (1997) conducted systematic velocity and boundary layer measurements by deploying four cylindrical cells of different aspect ratios ($\Gamma = 0.5$, 1, 2, and 4.4), with Ra varying from 10^7 to 10^{11}. Their results show

that the previous finding $\delta_\upsilon \sim Ra^{-0.16}$ holds for all Γ studied. They also defined a new boundary layer length scale (δ_σ), identified from the profiles of the velocity r.m.s., and found that $\delta_\sigma \sim Ra^{-0.25}$. In two separate studies, Qiu & Xia (1998*a*, *b*) measured the boundary layer thickness respectively at the sidewall and at the bottom plate of a cubic convection cell. Their results show that the scaling exponent of the boundary layer thickness measured at the sidewall is the same as those found for classical shear flows (their result gave $\delta_\upsilon \sim Ra^{-0.26\pm0.03}$, which implies $\delta_\upsilon \sim Re^{-0.52}$). On the other hand, at the bottom plate they found $\delta_\upsilon \sim Ra^{-0.18\pm0.04}$, which is essentially the same as in cylindrical cells (Xin *et al.* 1996; Xin & Xia 1997).

By measuring the degree of spatial correlation of temperature fluctuations between two thermistor probes placed perpendicular to the mean flow direction, Zhou & Xia (2001) were able to determine the viscous boundary layer thickness in a cylindrical Rayleigh–Bénard convection cell in water. The results obtained are in excellent agreement with those measured by the direct light-scattering technique. The technique takes advantage of the existence of a predominantly horizontal coherent mean flow near conducting plates and should be especially useful in fluids that are not easily accessible to optical methods, such as liquid metals and gases.

Using a combination of water and three alcohol-type organic liquids as the convecting fluids, Lam *et al.* (2002) measured both the *Ra*- and *Pr*-dependence of the viscous boundary layer thickness in a single cylindrical convection cell of unity aspect ratio. Over the range of *Ra* from 2×10^8 to 2×10^{10} and of *Pr* from 6 to 1027, they found that the normalized viscous layer thickness can be represented as $\delta_\upsilon/H = 0.65Pr^{0.24}Ra^{-0.16}$, where H is the cell height. Haramina & Tilgner (2004) studied boundary layers in a cubic convection cell filled with water using a dyeing technique at $Ra = 1.3\times10^9$. They report a new coherent structure in the boundary layer, which they suggest could be produced by pairs of counter-rotating vortices. In separate numerical studies of turbulent convection, Kerr & Herring (2000) and Verzicco & Camussi (2003) have investigated some statistical quantities of the boundary layer. However, to our knowledge, dynamic boundary layer quantities such as near-wall viscous shear tress and turbulent (Reynolds) shear stress have not been experimentally measured in convective turbulence. This lack of experimental data has prevented quantitative comparisons between the velocity boundary layer in thermal turbulent convection with those in shear flow turbulence. Most experiments measured only one velocity component in single-point measurements, and so statistical quantities concerning the correlation between different velocity components and the velocity difference at different positions have not been obtained.

1.5. *Application of PIV in turbulent thermal convection*

The technique of particle image velocimetry (PIV) is a convenient tool to directly visualize and measure the two-dimensional flow field in a particular plane of interest (Adrian 1991). In a PIV measurement one captures two consecutive two-dimensional images of the seed particles using a charge-coupled device (CCD) camera and then cross-correlates the two images to produce the displacement of each particle, from which one obtains the velocity map. The main advantage of the PIV method is its ability to follow the motion of a two-dimensional flow field. With the two-dimensional time series data, one can obtain both the time-averaged and the dynamic properties of the two-dimensional flow field.

In recent years, PIV has been used to measure the various properties of the velocity field in turbulent Rayleigh–Bénard convection in different cell geometries.

For example, Xia, Sun & Zhou (2003) measured the flow structure and statistical properties of the velocity field in the bulk fluid in a rectangular cell over a wide range of Ra (from 9×10^8 to 9×10^{11}). Their results show that the driving mechanism of the large-scale circulation is the buoyancy of the plumes instead of fluctuations or Reynolds stress associated with the plumes. It was also found that an inner-core and an outer-shell flow structure coexists in the system when Ra is larger than a critical value and that the two structures have different rotation frequencies with distinct Ra-scaling exponents. Burr, Kinzelbach & Tsinober (2003) measured statistical properties of velocity field in a cubic cell for $Ra = 1.61 \times 10^9$. Their results also suggests that the LSC is not driven by turbulent Reynolds stress.

Sun, Xia & Tong (2005*c*) made a comprehensive study of the three-dimensional structure of the flow field in an aspect-ratio-unity cylindrical cell, which revealed how thermal plumes have synchronized their emissions and organized their motions spatially between the top and bottom plates, leading to an oscillatory motion in the bulk region of the fluid with a period equal to twice the plume's cell-crossing time. Sun, Xi & Xia (2005*b*) studied the flow dynamics in an aspect ratio $\Gamma = 1/2$ cylindrical cell. Their results show how the azimuthal motion of the quasi-two-dimensional instantaneous flow structure produces a time-averaged three-dimensional flow pattern featuring two toroidal rings near the top and bottom plates. Their work also demonstrated that different flow states can indeed produce different global heat transport in a turbulent convection system. Xi *et al.* (2006) studied the azimuthal motion of the large-scale circulation in an aspect-ratio-unity cylindrical cell and found that the azimuthal motion consists of erratic fluctuations and a time-periodic oscillation. In high-resolution PIV measurements, Sun, Zhou & Xia (2006) obtained real-space velocity structure functions and found that they do not follow the Bolgiano–Obukhov scaling in both the central and the sidewall regions of the convection cell. In a more recent study, they investigated the small-scale statistical properties of the velocity circulation and found that the circulation is more sensitive to small-scale anisotropy than the velocity structure functions (Zhou, Sun & Xia 2008). Recently, Eidelman *et al.* (2006) studied the hysteresis phenomenon of the large-scale circulation in turbulent convection using PIV.

1.6. *Organization of the paper*

In this paper, we study the properties of the thermal and viscous boundary layers near the bottom plate of a rectangular cell. For the temperature field, both the time-averaged and r.m.s. profiles are obtained near the bottom plate. For the velocity field, high-resolution two-dimensional velocity measurements are made near the plate. In particular, we study the time-averaged, statistical and dynamical quantities of the viscous boundary layer. We also study the scaling properties of the temperature and velocity r.m.s. profiles with distance from the horizontal plate. The remainder of this paper is organized as follows. In § 2 we describe the experimental apparatus and measurement methods. Section 3 presents the experimental results, which are divided into nine subsections. In § 3.1 we present the measured temperature profiles and the temperature-dependent fluid properties as functions of the distance from the horizontal plate, which will be used to obtain the thermal boundary layer and the viscous and Reynolds stresses. In § 3.2, the measured velocity profiles and the viscous boundary layer thickness are presented. The viscous boundary layers based on two different definitions are also discussed. In § 3.3, the scaling of the Reynolds number Re with Ra is presented. In § 3.4, the scaling properties, with both Ra and Re, of

two kinds of boundary layer thicknesses, one determined from the mean velocity profile and the other determined from the r.m.s. velocity profile, are presented and discussed. We also discuss the influence of the geometry of the cell on the boundary layer scaling. In § 3.5 statistical properties (r.m.s. and skewness) of the velocity field in the boundary layer region are discussed. In § 3.6 we present the scaling, with distance, of the profiles of the temperature and velocity fluctuations in the mixing zone and discuss the difference between power-law and logarithmic profiles. Section 3.7 presents results of the viscous and Reynolds shear stresses distributions in the boundary layer and discusses their relative contributions to the total shear stress as functions of *Ra*. In § 3.8 we discuss the scaling, with both *Ra* and *Re*, of several boundary layer quantities, such as the friction velocity, the friction coefficient, and the wall thickness. Profiles of the mean and r.m.s. horizontal velocities normalized by wall units and for different values of *Ra* are also presented, and their properties are discussed with respect to those of classical shear flows. In § 3.9 we discuss possible implications of the present results by extrapolating them to much higher values of *Ra*. We summarize our findings and conclude in § 4.

2. Experimental apparatus and methods

2.1. *The convection cell*

The choice for the shape of the convection box is based on the following considerations. For the most widely used cylindrical shape, the curved sidewall will introduce distortions in the images viewed by the camera. Although this distortion can be partly corrected by fitting a square-shaped jacket round the sidewall of the convection cell, the jacket unavoidably limits the field of view in regions near the top and bottom plates. For a cube-shaped cell, it is known that the mean flow is confined in the diagonal plane of the box (Zocchi, Moses & Libchaber 1990; Qiu & Xia 1998*a*, *b*), which means that the PIV method will measure only a projection of the flow field. With these in mind, a rectangular shape is chosen for the convection box. Another important reason is that the rectangular cell enables us to achieve a very high resolution, because the shortest distance between the region of interest (measuring area) and the camera lens can be achieved compared with other shapes of comparable size. The length (L), width (W), and height (H) of the cell is $25 \times 7 \times 24$ (cm^3). With this geometry, the large-scale flow is largely confined in the plane with aspect ratio $\Gamma = L/H \simeq 1$, which is the circulation plane of the LSC, and the velocity in this plane will be the dominant component of the LSC (Xia *et al.* 2003).

The convection cell has been described in detail previously (Xia *et al.* 2003). Here we give only its essential features. The top and bottom conducting plates are made with pure copper and their fluid-contact surfaces are plated with a thin layer of gold. The sidewall is made of Plexiglas. The temperatures of the plates are monitored by four embedded thermistors, two in each one. The top plate temperature was maintained constant by a refrigerated circulator (Polyscience Model 9702) that has a temperature stability of 0.01 °C. Two silicon rubber film heaters connected in series are stuck to the back of the bottom plate to provide constant and uniform heating. A DC power supply (Xantrex XFR 300-4) with 99.99% long-term stability was used to heat the plate at a constant flux. The top and bottom parts of the cell are wrapped with nitrile rubber sheets for thermal insulation. With this setup, the cell's conducting plates have temperature stability and uniformity better than 1% of the temperature difference across the cell. It has been found that room temperature fluctuations could

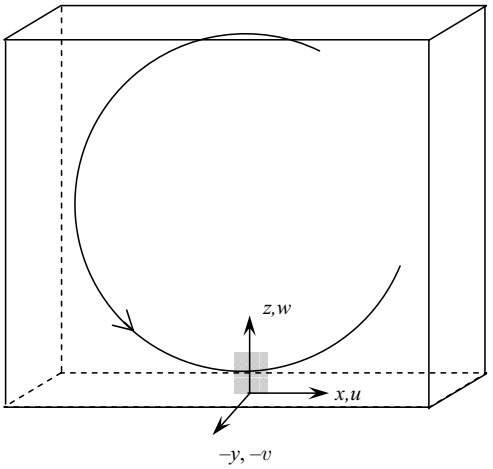

FIGURE 1. Sketch of the convection cell and the Cartesian coordinates used in temperature and velocity measurements. The shaded region represents the PIV measuring area.

influence the flow pattern and velocity distributions in the cell. It is therefore important that a constant-temperature environment be maintained. We achieved this by placing the entire convection cell inside a thermostat box whose temperature matched the mean temperature of the bulk fluid in the convection cell. The thermostat box reduces heat leakage and maintains a constant mean temperature of the working fluid in the cell so that it is not subjected to room temperature fluctuations. The constant mean temperature of the bulk fluid also implies a constant Prandtl number Pr. The temperature stability of the thermostat is better than 0.05 °C.

2.2. *The PIV measurements*

Figure 1 shows a sketch of the coordinates of the velocity measurements with respect to the cell geometry. The origin of the coordinates is chosen to coincide with the centre of the bottom plate. The x- and z-axes lie in the circulation plane of the large-scale circulation; the y-axis is perpendicular to the LSC-plane and points inward. The symbols u, v and w denote the instantaneous velocity components along the x-, y- and z- directions, respectively. Near the bottom plate u is the main velocity component. The PIV system consists of a dual neodymium-doped yttrium aluminum garnet (Nd:YAG) laser operated at a power of 80 mJ per pulse, lightsheet optics, a cooled CCD camera with 12-bit dynamic range and a spatial resolution of 1280 × 1024 pixels, a synchronizer, and control software, which contains a PIV data analysis package (TSI, Inc.). A laser lightsheet of thickness $\simeq$ 0.2 mm is used to illuminate the seed particles in the plane of interest (the x, z-plane). The seed particles used in the experiments are 2.89 μm diameter polyamid spheres (density 1.03 g cm^{-3}). This particle size is chosen such that its image roughly occupies the area of one pixel in the CCD sensor, which is the optimal size for the present experiment (Xia *et al.* 2003; Sun *et al.* 2005*c*).

The two-dimensional velocity map is obtained by cross-correlating two consecutive images taken at a time interval ranging from several hundred to several thousand μs according to the value of Ra and is optimally selected for the corresponding flow speed. The selection criterion for the delay time is set such that most particles move across several pixels during the time interval. To achieve more data points in

the z-direction, we oriented the CCD in such a way that it has 1280 pixels in the z-direction and 1024 pixels in the x-direction. Each two-dimensional velocity vector is calculated from a subwindow (32 pixels $\times$ 32 pixels) that has 50% overlap with its neighbouring subwindows (Adrian 1991), so each vector corresponds to a region of 16 pixels $\times$ 16 pixels and each velocity map contains 63 and 79 velocity vectors in the x- and z-directions respectively. Because the number of pixels in the CCD is fixed, the view area should be made as small as possible to achieve high spatial resolution. By installing several extension tubes between the CCD and the lens, a rectangular measuring area with dimensions $x = 11.07$ mm and $z = 13.84$ mm was achieved. The spatial resolution is 0.17 mm in both the x- and the z-directions, which is smaller than both the Kolmogorov scale and the thermal boundary layer thickness ($\eta = 0.4$ mm and $\delta_{th} = 0.58$ mm for the highest $Ra = 2.5 \times 10^{10}$) in the present experiment.

2.3. *Experimental conditions and parameters*

Water was used as the convecting fluid and the experiment was conducted at $Pr = 4.3$, which corresponds to a mean bulk fluid temperature of 40.0 °C. The cell was levelled in all measurements (better than 0.1°). By changing the temperature difference between the top and the bottom plates, we varied Ra from 1.25×10^9 to 2.5×10^{10} while keeping Pr constant. For each Ra, 30 000 vector maps were acquired at a sampling rate of 2.2 Hz in a single measurement of duration 3.79 h.

3. Results and discussion

3.1. *Temperature profiles and fluid properties*

The boundary layer in turbulent thermal convection is rather complex, because both velocity and thermal boundary layers are present and they influence each other. For example, the intermittent emission of thermal plumes (which are believed to be detached from thermal boundary layers) will modify the viscous boundary layer, while the shear of the horizontal velocity that sweeps over the plates helps to stabilize the thermal boundary layer. Although the primary objective of the present work is to study the properties of the viscous boundary layer, we also measured temperature profiles near the plate, and hence the thermal boundary layer. Profiles of the mean temperature and its fluctuations for each Ra (from 10^9 to 10^{10}) were measured, mainly because the viscous shear stress and Reynolds stress depend respectively on the viscosity and density of the fluid, and these quantities have strong temperature dependences.

The experimental method and apparatus used in the temperature profile measurements are similar to those described previously by Lui & Xia (1998) and Wang & Xia (2003), except that the thermistor probe in the present case traverses only vertically but not horizontally. We measured the mean temperature and its fluctuations for different z along the central axis ($x = y = 0$) of the cell. In figure 2 we show examples of the mean temperature and its fluctuation profiles at $Ra = 1.07\times10^{10}$. As temperature in the bulk region is a constant of position, we measured only the part of the temperature profile from the plate to $z = 40$ mm (the height of the cell is 240 mm), and for clarity only the part between $z = 0$ and $z = 20$ mm is shown in figure 2. It is seen that the mean temperature drops dramatically with increasing distance from the bottom plate in a very limited region, and the temperature quickly becomes constant outside the boundary layer region. As shown in figure 2(a), the thermal boundary layer thickness δ_{th} is defined as the distance from the wall at which the extrapolation of the linear part of the temperature profile meets the horizontal

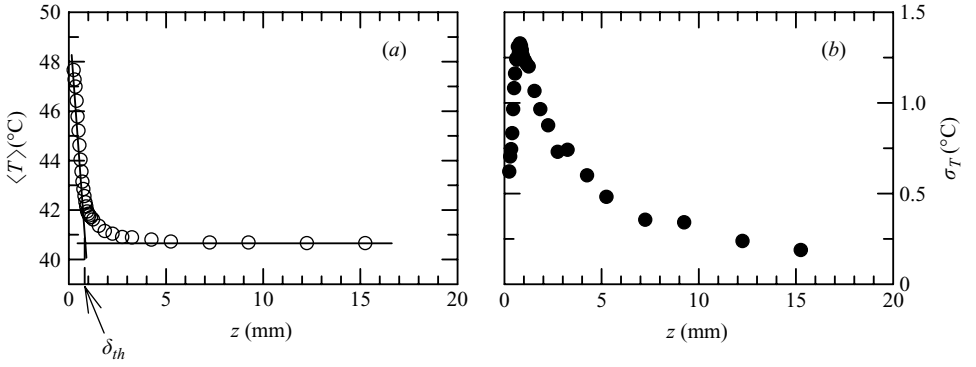

FIGURE 2. Typical mean temperature $\langle T \rangle$ and r.m.s. temperature σ_T profiles ($Ra = 1.07 \times 10^{10}$). Definition of the thermal boundary layer thickness δ_{th} is also illustrated.

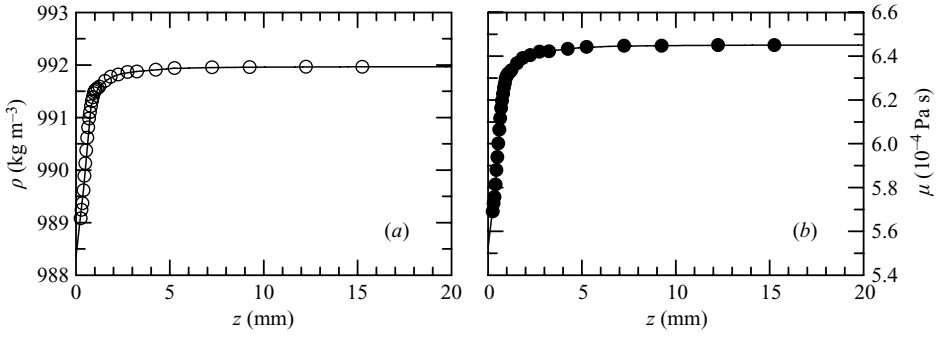

FIGURE 3. Typical density ρ and dynamic viscosity μ profiles of the convecting fluid (water) obtained from the mean temperature profile ($Ra = 1.07 \times 10^{10}$). Lines in the figure are data smoothed with a negative exponential smoother.

line passing through the bulk temperature of the system. This definition is the same as that in Lui & Xia (1998), which is based on the slope of the mean temperature profile near conducting plate. The boundary layer thickness at this Ra (1.07×10^{10}) is $\delta_{th} = 0.75$ mm based on this definition.

The Ra-scaling properties of the thermal boundary layer will be presented in § 3.4, together with those of the viscous boundary layer. As shown in figure 2(*b*), the r.m.s. increases with increasing z when z is very small and reaches a maximum, then decreasing with increasing distance from the plate. The r.m.s. temperature (σ_T) will be discussed in detail in § 3.6. From the temperature profiles, we can also calculate the density and viscosity profiles for different Ra using the published properties of water (Yaws 1999). Figure 3 shows examples calculated from the mean temperature profile in figure 2 ($Ra = 1.07 \times 10^{10}$). It is seen that both the density and viscosity of the working fluid have strong position dependence in the region of the thermal boundary layer (i.e. the region of steep temperature gradient). Obviously, local values of these fluid properties will have to be used in the calculation of the position-dependent viscous and Reynolds shear stresses.

3.2. *Mean velocity profile and determination of the viscous boundary layer*

We now present results from the velocity measurements. We first examine the velocity field near the plate. Figure 4(*a*) shows an instantaneous two-dimensional velocity map

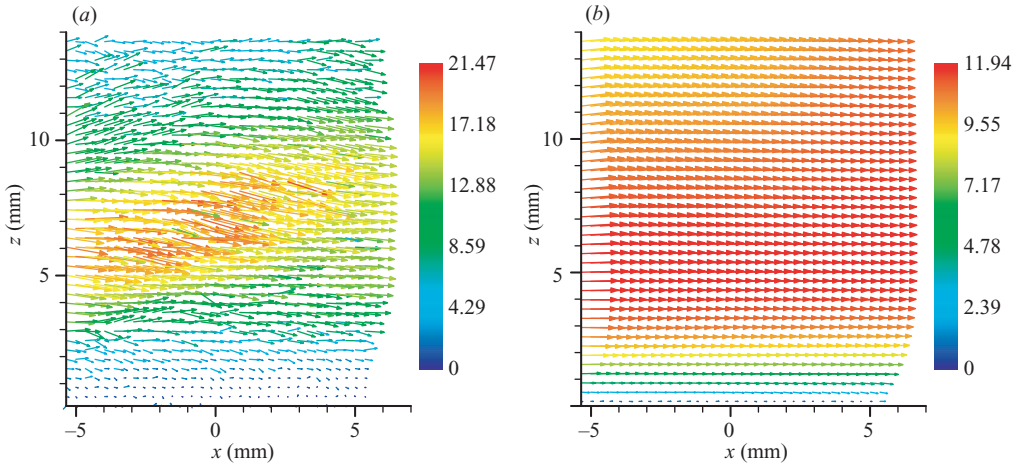

FIGURE 4. Coarse-grained vector maps of the instantaneous (*a*) and time-averaged (*b*) velocity field measured near the centre of the bottom plate ($Ra = 5.3 \times 10^9$). The magnitude of the velocity is coded in both colour scale and the length of the arrows in unit of mm s^{-1}. Note that a laminar boundary layer about 2 mm in thickness is apparent from both the instantaneous and the time-averaged velocity fields.

measured at $Ra = 5.3 \times 10^9$ and figure 4(*b*) shows the time-average of the same velocity field taken over a period of 3.79 h (corresponding to 30 000 velocity frames). In the present measurements, x spans from -5.36 mm to 5.36 mm, and z spans from 0 to 13.49 mm. Note that, to improve readability, both plots in figure 4 have been coarse-grained (by combining every four vectors into one), so the apparent spatial resolution in the figure is less than the actually measured one. From figure 4 it is seen that the time-averaged velocity field in the boundary layer region is laminar while the instantaneous velocity map shows velocity bursts much higher than the mean value (notice the difference in the velocity scales in the two figures). In particular, the large velocity burst in the centre of figure 4(*a*) presumably corresponds to the emission of a thermal plume or a cluster of plumes. As the mean velocity and the velocity fluctuations are found to be independent of the horizontal position x over the range of the measurements, all quantities presented below are based on values averaged along the x- direction over the width of the measuring area, which leads to an increased statistical accuracy of the measured quantities.

Figure 5 shows the time-averaged horizontal and vertical velocities, $U(z) = \langle u(z,t)\rangle$ and $W(z) = \langle w(z,t)\rangle$, as functions of the vertical distance z. From the figure, we can see that the main velocity component $U(z)$ has the following characteristics: it increases linearly close to the plate, and after reaching the maximum value U_{max} it decays as z increases towards the central region of the cell. Note that $W(z)$ is zero at $z = 0$ because of the impermeability condition, and $U(z)$ is zero at $z = 0$ because the non-slip boundary condition holds in this system, at least the slip length can be neglected. There are quite a few definitions of the viscous (or velocity) boundary layer thickness, among which two are commonly used (Schlichting & Gersten 2000). In the first the boundary layer thickness δ_v is defined as the distance from the wall at which the extrapolation of the linear part of the horizontal velocity profile meets the horizontal line passing through the maximum horizontal velocity U_{max}. As shown in figure 5, the boundary layer defined in this way gives $\delta_v = 2.30$ mm for the given Ra. An alternative definition of the boundary layer thickness is the distance from the

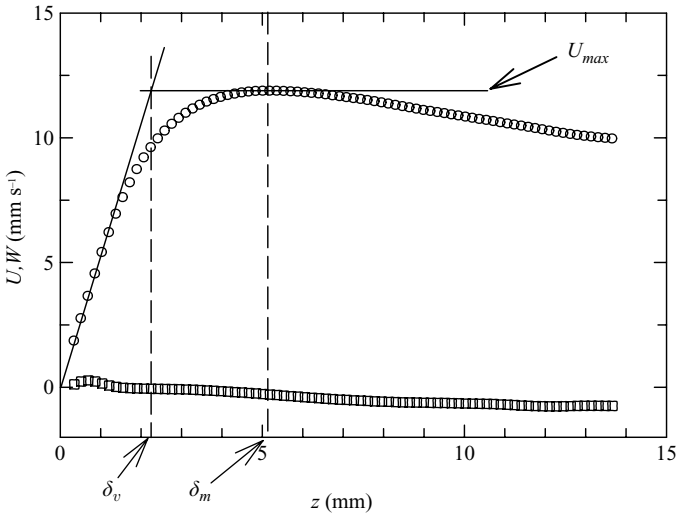

FIGURE 5. Profiles of the time-averaged horizontal U (○) and vertical W (□) velocities measured near the bottom plate ($Ra = 5.3 \times 10^9$). The solid and dashed lines illustrate two different definitions of the velocity/viscous boundary layer.

wall at which the velocity is 99% of its maximum amplitude. The rationale for this second definition is that in traditional shear flows the transition from boundary-layer flow to outer flow is continuous, so that it is difficult to find the position of maximum velocity. As can be seen from figure 5, in the Rayleigh–Bénard system the position of maximum velocity can be easily determined. So we revise the second definition of boundary layer thickness. The thickness δ_m is now defined as the distance between the wall and the position at which the horizontal velocity $U(z)$ is maximum. It is seen from figure 5 that the boundary layer so defined gives $\delta_v = 5.19$ mm for the given Ra. As shown by figure 4, a 'boundary layer thickness' of about 2 mm (hence δ_v) is physically more reasonable and therefore δ_v seems to be a better choice. In § 3.4 we will discuss the scaling properties of the two boundary layer length scales and decide which of the two definitions of thickness will be adopted in our study. Figure 6 plots the velocity profiles for eight different values of Ra. From the un-normalized profiles shown in figure 6(a) we can see that the shape of the profiles is rather similar even though their amplitudes are not equal. Figure 6(b) plots the normalized profiles in which $U(z)$ is normalized by the maximum horizontal velocity $U_{max}(Ra)$ and the distance z from the wall by the viscous boundary layer thickness $\delta_v(Ra)$. It shows clearly that all profiles for different Ra collapse onto a single curve quite well, suggesting a universal profile of the laminar boundary layer for different values of Ra.

3.3. *Scaling of the Reynolds number*

Because the LSC is the largest flow structure in the system, its velocity may be used to define the Reynolds number of the system. The key to the definition of the Reynolds number Re is the selection of a typical velocity of the system. Here we use the velocity U_{max} where the horizontal velocity is maximum in the profile (see figure 5), i.e. $Re = U_{max}H/\nu$. In Sun & Xia (2005) it was shown that near the sidewall of the convection cell there exist occasional flows opposite to the overall LSC flow direction, which could be caused by some energetic plumes travelling in the 'wrong direction' along the sidewall. When this counterflow becomes significant it reduces the value of

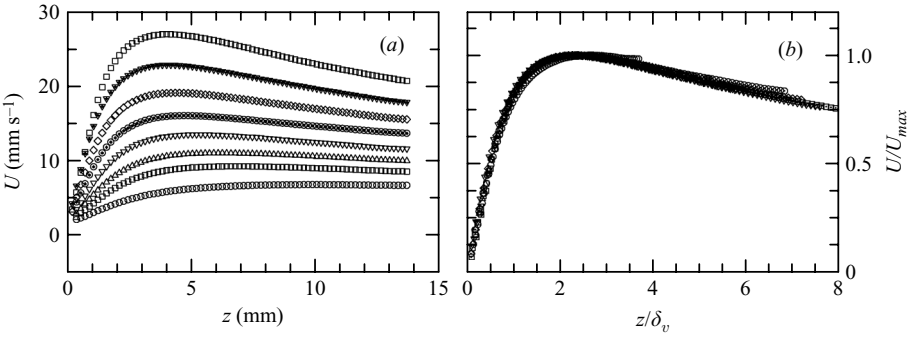

FIGURE 6. (*a*) Time-averaged horizontal velocity profiles measured at eight different Ra, from bottom to top: $Ra = 1.25 \times 10^9$, 2.34×10^9, 3.43×10^9, 5.30×10^9, 7.53×10^9, 1.07×10^{10}, 1.52×10^{10} and 2.02×10^{10}. (*b*) Profiles in (*a*) normalized by their respective maximum velocity $U_{max}(Ra)$ and viscous boundary layer thickness $\delta_\upsilon(Ra)$.

the mean velocity, which will then no longer be representative of the strength of the LSC. In such a case it has been shown that the proper value to use for the Reynolds number is the most probable value of the velocity distribution (Sun & Xia 2005). In the present case, however, the measurements were made near the bottom plate of the cell and no significant counterflow exists. This can be seen from the histograms of u measured at the position of maximum velocity, which are shown in figure 7 for several values of Ra. So here we simply use the time-averaged maximum velocity U_{max} for the Reynolds number Re.

In figure 8 we show Re *vs* Ra in a log-log plot, where the solid line represents the best power-law fit $Re = 0.0184Ra^{0.55\pm0.01}$. The inset of the figure is a compensated plot of the same data, which shows that 0.55 is indeed an excellent exponent to describe the data. We are not aware of any theoretical model that predicts a Reynolds number scaling exponent larger than 0.5, but previous experiments have also found a value larger than 0.5 (although for different Pr fluids). For example, Lam *et al.* (2002) found in a cylindrical cell that the same exponent varies from 0.5 to 0.68 with Pr varying from 51 to 1027. It should also be mentioned that the scaling of Re with Ra has also been highlighted, although focused on different aspects, in several recent papers (Brown, Funfschilling & Ahlers 2007; Xia 2007). Thus, further studies, both experimental and theoretical, are needed to settle this issue.

3.4. *Scaling of the boundary layer thickness*

We now discuss the scaling of the boundary layer thickness with both the Rayleigh number Ra and the Reynolds number Re, and compare results based on the two different definitions of the boundary layer thickness as discussed in § 3.2. Figure 9(*a*) plots the Ra-dependence of the boundary layer thicknesses normalized by the cell height H. The solid circles represent δ_υ/H and the open circles represent δ_m/H. The solid lines in the figure represent best power-law fits to the respective data and give $\delta_\upsilon/H = 4.95Ra^{-0.27\pm0.01}$ and $\delta_m/H = 10.84Ra^{-0.27\pm0.01}$. Figure 9(*b*) plots the Re-dependence of δ_υ/H and δ_m/H with the same symbols. Again, the solid lines are power-law fits to the respective data, with $\delta_\upsilon/H = 0.64Re^{-0.50\pm0.03}$ and $\delta_m/H = 1.43Re^{-0.50\pm0.02}$. It is seen that the two boundary layer thicknesses defined differently have the same scaling behaviour with respect to both Ra and Re but their magnitudes differ by roughly a factor of 2, with δ_m being the larger. As discussed in

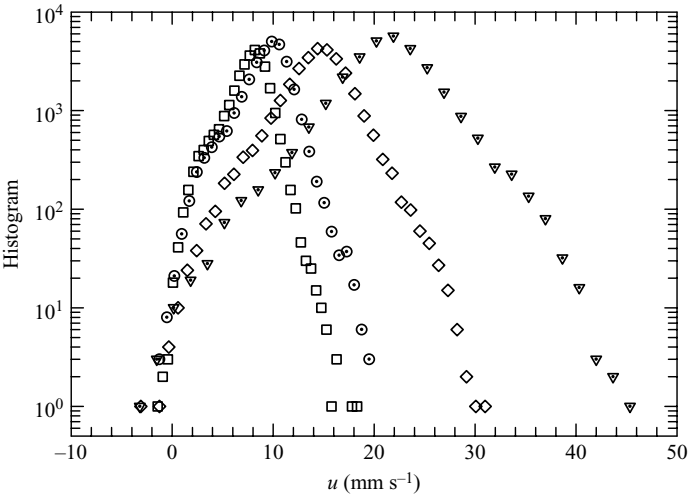

FIGURE 7. Histograms of the horizontal velocity $u(t)$ measured at the position of maximum velocity for four different values of Ra. Squares: $Ra = 2.34 \times 10^9$; circles with dots: $Ra = 3.43 \times 10^9$; diamonds: $Ra = 7.53 \times 10^9$; triangles with dots: $Ra = 1.52 \times 10^{10}$.

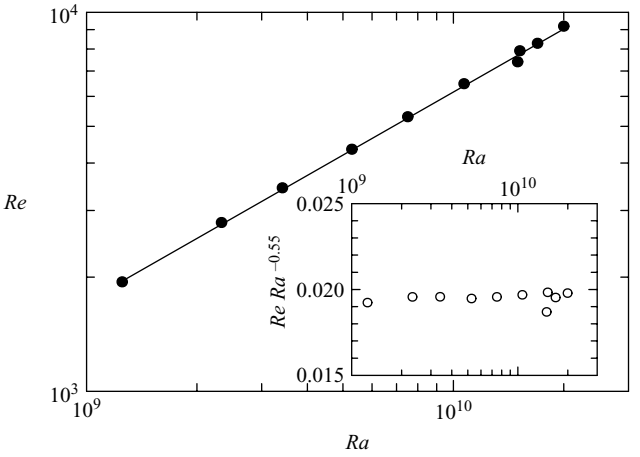

FIGURE 8. Ra-dependence of the Reynolds number based on the maximum horizontal velocity, i.e. $Re = U_{max} H/\nu$. The solid line represents the best power-law fit $Re = 0.0184 Ra^{0.55 \pm 0.01}$. The inset plots a compensated Reynolds number $ReRa^{-0.55}$ *vs* Ra.

§ 3.2, figure 4 suggests that δ_υ is a better choice and it is also the one that has been used most frequently in thermal convection studies (Belmonte *et al.* 1993; Xin *et al.* 1996; Xin & Xia 1997; Qiu & Xia 1998*a*, *b*), so it will be adopted as the velocity boundary layer in the present study.

The Re-scaling exponent of -0.5 of the velocity boundary layer is in excellent agreement with the predictions for Blasius-type boundary layers. However, the result appears to be inconsistent with previous experimental results obtained in cylindrical and cubic cells, which give $\delta_\upsilon \sim Ra^{-0.16}$ (Xin *et al.* 1996; Xin & Xia 1997; Qiu & Xia 1998*b*; Lam *et al.* 2002). Using the scaling relation $Re \sim Ra^{0.5}$ reported in those studies implies $\delta_\upsilon \sim Re^{-0.32}$. While we do not know the exact reason(s) for this

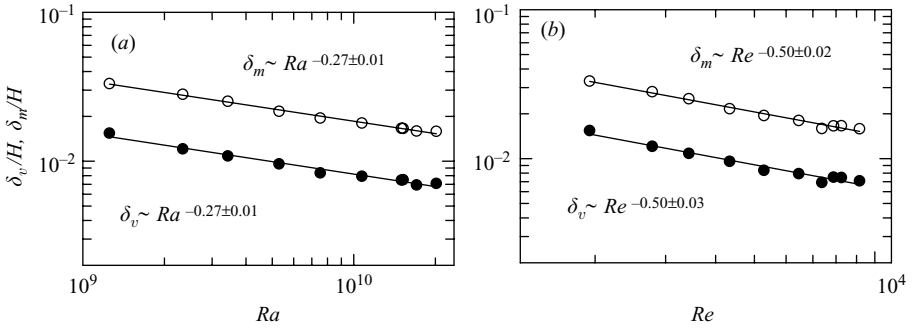

FIGURE 9. The scalings of normalized viscous boundary layer thicknesses with (*a*) the Rayleigh number Ra and (*b*) the Reynolds number Re, on a log-log scale. The open circles represent the thickness δ_m defined by the position of the maximum velocity and the solid circles represent the thickness δ_v defined as the distance at which the extrapolation of the linear part of the horizontal velocity profile equals the maximum horizontal velocity U_{max}.

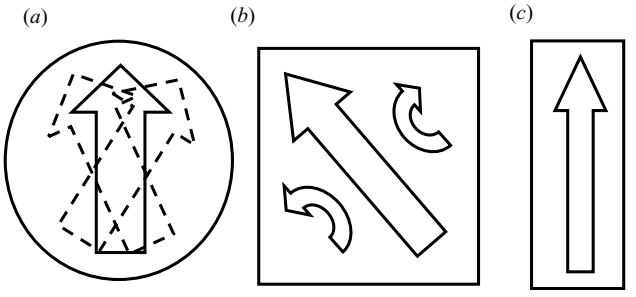

FIGURE 10. Sketches of the large-scale circulation in different cell geometries. (*a*) Cylindrical cell. (*b*) Cubic cell. (*c*) Rectangular cell.

discrepancy, we note that the viscous boundary layer is created by the shear of the LSC, which is different in different cell geometries. In the case of a cylindrical cell, it is known that the orientation of the LSC oscillates azimuthally (Sun *et al.* 2005*b*; Brown, Nikolaenko & Ahlers 2005; Xi *et al.* 2006) so that a steady shear is not always present. In the cubic cell the LSC near the horizontal conducting plate is along the diagonal. While it is not known whether the LSC also has orientational oscillations in the cubic geometry, it was found in Qiu & Xia (1998*b*) that there exist secondary flows that sometimes have opposite directions to the main LSC direction and these secondary flows could affect the stability of the main LSC. Recently, Zhou, Sun & Xia (2007*b*) have made local temperature and velocity measurements in a cell of similar geometry as the present one ($81 \times 20 \times 81\,\mathrm{cm}^3$ *vs* $25 \times 7 \times 24\,\mathrm{cm}^3$). They observed no velocity oscillations and only weak temperature oscillations near the bottom plate; while near the sidewall both velocity and temperature oscillations were observed, though much weaker than those seen in cylindrical cells. In figure 10 we illustrate the flow patterns of the LSC near the bottom plate for the various geometries and it is seen that the present rectangular geometry has the most stable flow structure among the three geometries. (Previous measurements have shown that the flow will align with the largest diagonal of the system when Ra becomes very high (Xia *et al.* 2003). In the present system, the depth of the cell is rather small comparing to its length, so this is a small effect. For simplicity, this is not illustrated in figure 10.) In the classical

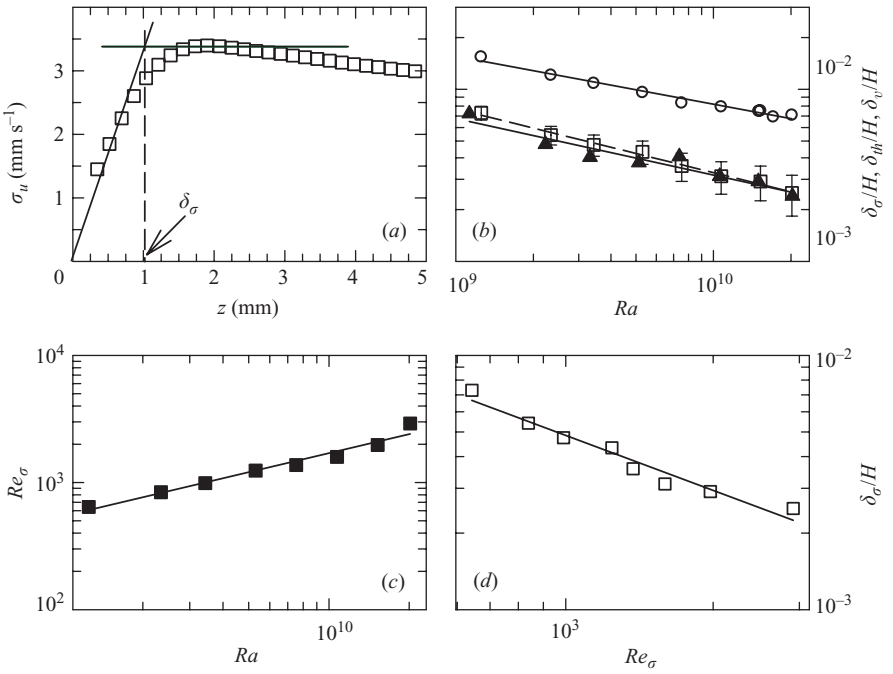

FIGURE 11. (*a*) Profile of the r.m.s. (σ_u) horizontal velocity component measured at $Ra = 5.3 \times 10^9$, the lines are used to illustrate the definition of the r.m.s. velocity-based viscous boundary layer thickness δ_σ. (*b*) Ra-dependence of δ_σ (squares), thermal boundary layer thickness δ_{th} (triangles) and viscous boundary layer thickness δ_υ (open circles). The fitting results are $\delta_\sigma/H = 16.5Ra^{-0.37\pm0.10}$, $\delta_{th}/H = 6.10Ra^{-0.32\pm0.05}$, and $\delta_\upsilon/H = 4.95Ra^{-0.27\pm0.01}$, respectively. (*c*) Ra-dependence of the Reynolds number $Re_\sigma = \sigma_u^{max} H/\nu$ based on maximum r.m.s. velocity, and the power-law fit gives $Re_\sigma = 0.018Ra^{0.50\pm0.04}$. (*d*) Re_σ-dependence of δ_σ. The power-law fit gives $\delta_\sigma/H = 0.69Re_\sigma^{-0.72\pm0.14}$.

theory of boundary layers, including the Blasius boundary layer, a steady shear is considered. This is also the case considered in the GL theory. If the smaller exponent measured in the cylindrical and cubic cells is indeed due to an unsteady shear, then a modification of the boundary layer theory for the case of unsteady shears would be needed.

In addition to the boundary layer thickness δ_υ that is defined based on the mean horizontal velocity profile, another length scale can also be defined based on the profile of the horizontal r.m.s. velocity σ_u, which may be called the r.m.s. velocity boundary layer thickness. The definition of this length scale, δ_σ, is illustrated in figure 11(*a*), which is similar to that of δ_υ. This scale was first introduced by Xin & Xia (1997), in which it was found that $\delta_\sigma \sim Ra^{-0.25\pm0.02}$ in a cylindrical geometry with aspect ratio varying from 0.5 to 4.4. In a later study, Qiu & Xia (1998*b*) found that $\delta_\sigma \sim Ra^{-0.22\pm0.04}$ in a cubic cell. It was also found that in both of these geometries the magnitude of δ_σ is intermediate between the viscous boundary layer δ_υ and the thermal boundary layer δ_{th}. In figure 11(*b*) we show the Ra-scaling of the r.m.s. velocity boundary layer thickness δ_σ (squares) from the present experiment. For comparison, δ_υ (circles) and δ_{th} (triangles) from the present work are also shown. Here, the thermal layer thickness δ_{th} is determined from the measured mean temperature profiles as discussed in § 3.1. The power-law fits give $\delta_\sigma/H = 16.5Ra^{-0.37\pm0.10}$ (dashed

Quantity	*Ra* range	*Pr*	Geometry	Bottom	Sidewall	Source
δ_υ	$10^8 \sim 10^{10}$	~ 7	Cylindrical	-0.16		a
	$10^7 \sim 10^{11}$	~ 7	Cylindrical	-0.16		b
	$10^8 \sim 10^{10}$	~ 7	Cubic	-0.16	-0.26	c
	$10^8 \sim 10^{10}$	6–1027	Cylindrical	-0.16		d
	$10^9 \sim 10^{10}$	4.3	Rectangular	-0.27		e
δ_σ	$10^7 \sim 10^{11}$	~ 7	Cylindrical	-0.25		b
	$10^8 \sim 10^{10}$	~ 7	Cubic	-0.26	-0.38	c
	$10^9 \sim 10^{10}$	4.3	Rectangular	-0.37		e

TABLE 1. Exponents of scaling, with *Ra*, for the viscous boundary layer thickness (δ_υ) and the r.m.s. velocity-based boundary layer thickness (δ_σ) for different geometries. The sources are: a. Xin *et al.* (1996); b. Xin & Xia (1997) (aspect ratio $\Gamma = 0.5$, 1, 2 and 4.4.); c. Qiu & Xia (1998*a*,*b*); d. Lam *et al.* (2002); e. present work.

line) and $\delta_{th}/H = 6.10Ra^{-0.33\pm0.05}$ (solid line) (and $\delta_\upsilon/H = 4.95Ra^{-0.27\pm0.01}$ as already discussed).

Several features are worthy of note. The first is that both the magnitude and the *Ra*-scaling exponent of δ_σ are very close to those of the thermal layer. In fact, within the experimental uncertainties, δ_σ and δ_{th} may be regarded as the same. In contrast, in the cylindrical and cubic geometries, the magnitude of δ_σ is intermediate δ_υ and δ_{th}. We think this suggests a stronger coupling between the temperature and velocity fluctuations in the rectangular geometry, but do not understand why this should be the case. The second feature is that the scaling exponent of δ_σ, like that of δ_υ, is quite different from the other two geometries. It is interesting that the exponents of δ_σ and δ_υ for the rectangular case are the same (again within experimental error) as those found near the sidewall of a cubic cell (Qiu & Xia 1998*a*) and that for all three geometries the absolute value of the exponent of δ_σ is always larger than that of δ_υ by 0.1.

For ease of reference, we summarize the exponents of the two boundary layer length scales in table 1. They were measured near both the bottom plate and sidewall for the various geometries (where applicable) and over different ranges of *Ra* and *Pr*. The maximum value in the r.m.s. velocity profile, σ_u^{max} may also be used to define an r.m.s. velocity-based Reynolds number: $Re_\sigma = \sigma_u^{max} H/\nu$. The *Ra*-dependence of Re_σ is plotted in figure 11(*c*), where the solid line represents a power-law fit to the data: $Re_\sigma = 0.018Ra^{0.50\pm0.04}$. This result is consistent with similar results found for the other two geometries (Xin & Xia 1997; Qiu & Xia 1998*a*, *b*). In figure 11(*d*) the dependence of δ_σ on Re_σ is plotted, which is obtained using the relation between Re_σ and *Ra*. The power-law fit gives $\delta_\sigma/H = 0.69Re_\sigma^{-0.72\pm0.14}$.

3.5. *Statistical properties of the velocity field in the boundary layer*

As already mentioned, to our knowledge there are no experimental measurements of the statistical properties of the velocity field inside the boundary layer in turbulent thermal convection. A careful and comprehensive analysis of the statistical properties of the velocity field, such as its r.m.s. and skewness values may thus shed light on the complex turbulent convection problem.

Figure 12 shows the time series of both the horizontal component $u(t)$ (left panels) and the vertical component $w(t)$ (right panels) of the velocity, measured at various positions from the plate. The corresponding velocity histograms are shown in figure 13.

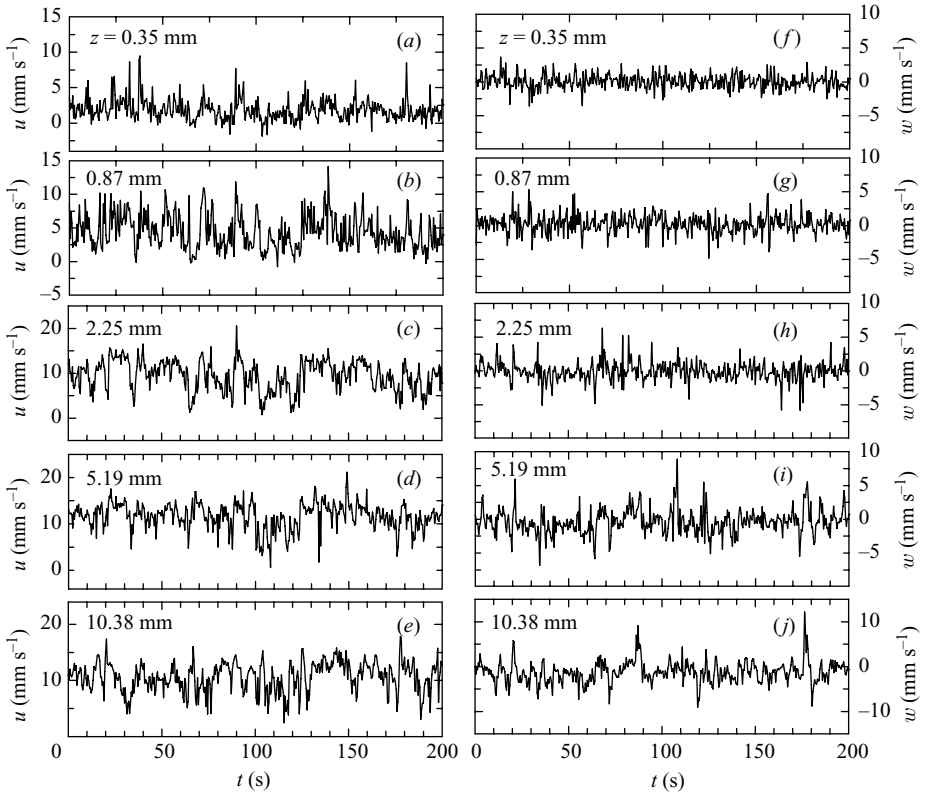

FIGURE 12. Time traces of horizontal $u(t)$ (left panels) and vertical $w(t)$ (right panels) velocity components measured at $Ra = 5.3 \times 10^9$ and at $x = 0$ and different distances z from the bottom plate.

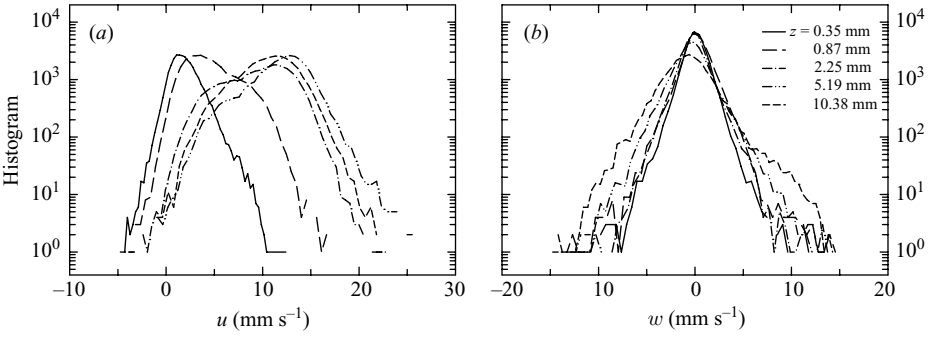

FIGURE 13. Histograms of (*a*) the horizontal $u(t)$ and (*b*) vertical $w(t)$ velocity components at various distances from the bottom plate measured at $Ra = 5.3 \times 10^9$.

The measurements were made at $Ra = 5.3 \times 10^9$. At this value of Ra, the thermal boundary layer thickness $\delta_{th} \approx 0.9$ mm, the velocity boundary layer thickness $\delta_\upsilon = 2.3$ mm and the maximum velocity $U_{max} = 11.87\,\mathrm{mm\,s^{-1}}$ (at $z = 5.19$ mm). The results shown in figures 12 and 13 therefore correspond to several typical positions: (i) inside the thermal boundary layer, (ii) around the thermal boundary layer, (iii) around the viscous boundary layer; (iv) at the position of the maximum velocity; and (v) far away from the boundary layers. The figures show that overall the horizontal velocity is the

dominant component, and that for positions near or below the thermal boundary layer it is skewed toward higher velocity values. But for positions near or above the viscous boundary layer the horizontal velocity is skewed toward smaller velocity values (i.e. negative skewness). The vertical velocity, on the other hand, shows similar behaviour at the different positions, i.e. fluctuates around zero with no significant asymmetry and the amplitude of fluctuations increases with increasing distance from the plate.

Figure 12(*a*) shows the horizontal velocity very close to the plate ($z = 0.35$ mm). The position is well within both the thermal and velocity boundary layers and the velocity amplitude is very small but there are intermittent bursts toward the positive side (i.e. the velocity is skewed toward the mean flow direction).

Around the position of the thermal boundary layer (figure 12*b*, $z = 0.87$ mm), we can see clearly that there are quite number of velocity bursts toward the direction of the mean flow, in addition to the increased fluctuations. It is generally believed that plumes are produced as a result of thermal boundary layer detachments or instabilities. So it is reasonable to associate the observed velocity bursts at thermal boundary layer with emissions of thermal plumes. Note that the number of bursts (plumes) in the horizontal velocity is much larger than in the vertical velocity measured at the same position (figure 12*g*). This implies that the plumes are swept predominantly in the horizontal direction after they are emitted.

When z is further increased to 2.25 mm (figure 12*c*), which corresponds to the position of the velocity boundary layer, both the mean and the standard derivation of the velocity become much larger than at the previous two positions. At $z = 5.19$ mm the mean velocity is maximum, and both the time series and the histogram exhibit the same features as measured far away from the boundary layer ($z = 10.38$ mm). They also have the same characteristics of the LSC in the interior of the cell obtained in a previous study (Xia *et al.* 2003). A notable feature of the horizontal velocity histograms shown in figure 13(*a*) is that they appear to be the superpositions of two contributions, resulting in two peaks. This is most likely caused by a fluctuating boundary layer so that the measurement point is sometimes inside and sometimes outside the boundary layer. Obviously, the relative weightings of the two components change with the measurement position. To disentangle these two components from the measured velocity data requires more systematic measurement and will be the subject of future studies.

The statistical properties of the velocity may be characterized more quantitatively by its root-mean-square (r.m.s.) value and its skewness, which are shown in figure 14. Figure 14(*a*) plots the velocity r.m.s. σ_u (solid circles) and σ_w (open circles) versus the normalized distance z/δ_υ. In figure 14(*b*) the skewness profiles, also versus z/δ_υ, are plotted, where the solid squares represent the horizontal velocity skewness $S_u \equiv \langle (u - \langle u \rangle)^3 \rangle / (\langle (u - \langle u \rangle)^2 \rangle)^{3/2}$ ($\langle \cdots \rangle$ denotes the time-average) and the open squares represent the vertical velocity skewness $S_w \equiv \langle (w - \langle w \rangle)^3 \rangle / (\langle (w - \langle w \rangle)^2 \rangle)^{3/2}$ (for σ_w we discuss here only its general features; its other properties, together with the profiles of the temperature r.m.s., will be discussed in the next subsection). Figure 14 shows that initially both σ_u and σ_w increase with increasing distance from the plate, with σ_w reaching its maximum value around $0.5\delta_\upsilon$ and σ_u around $0.7\delta_\upsilon$, and then decrease as z increases. Outside δ_υ, the r.m.s. was influenced by the outer flow. The skewness of the horizontal velocity S_u is seen to reach its maximum value very near the wall (even inside the thermal boundary layer). It then decreases to a negative value near the viscous boundary layer and levels off afterwards. This may be explained by the fact that very close to the wall, fluctuations against the mean flow are severely restricted

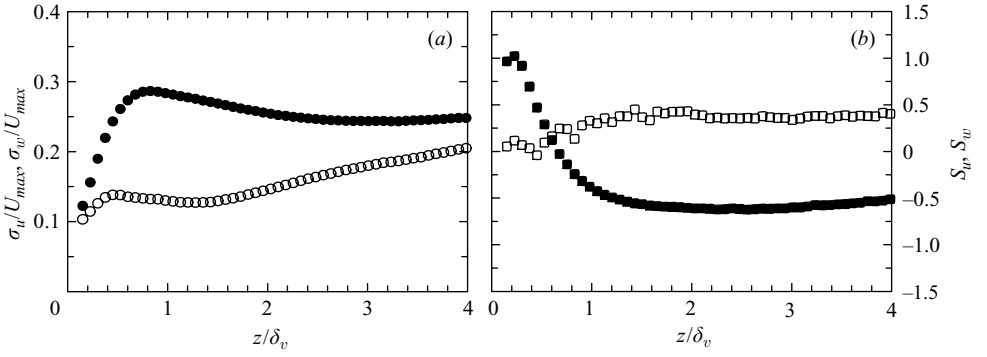

FIGURE 14. (*a*) The normalized r.m.s. σ and (*b*) skewness S profiles measured at $Ra = 5.3 \times 10^9$. Solid symbols: those of u; open symbols: those of w. The vertical distance z is normalized by the velocity boundary layer thickness δ_v.

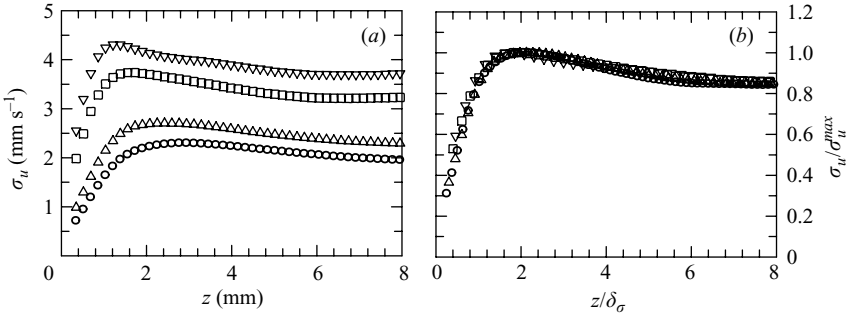

FIGURE 15. (*a*) The measured r.m.s. (σ_u) horizontal velocity profiles for different values of Ra, from bottom to top: $Ra = 2.34 \times 10^9$, 3.43×10^9, 7.53×10^9 and 1.07×10^{10}. (*b*) The normalized r.m.s. (σ_u/σ_u^{max}) *vs* normalized z ($= z/\delta_\sigma$) for the same Ra as in (a).

due to the strong shear. The skewness of the vertical velocity S_w is seen to remain more or less constant over the same distance. This feature can also be seen from the histograms of w (figure 13).

Next we examine the evolution of the horizontal r.m.s. and skewness velocity profiles with Ra. Figure 15(*a*) plots several profiles of σ_u for various values of Ra and figure 15(*b*) shows the same profiles normalized by the maximum r.m.s. velocity σ_u^{max} and the r.m.s. velocity boundary layer δ_σ (note that in figure 14, z is normalized by δ_v as both horizontal and vertical components are presented, and here z is normalized by δ_σ which is based on the horizonal r.m.s. velocity). The nearly perfect collapse of the profiles shows that δ_σ is a relevant length scale for the r.m.s. velocity field. In figure 16 we show the evolution of the normalized S_u profiles with Ra. An interesting feature is that, as Ra increases, a dip (most negative S_u) develops near the viscous boundary layer thickness and a hump (the value of S_u close to zero) also develops. This feature appears to emerge for $Ra \geqslant 7.5 \times 10^9$ but both the position of the dip ($\sim \delta_v$) and that of the hump ($\sim 2.5\delta_v$) appear to be insensitive to Ra once they appear. It is not clear what causes this, but we note that around $Ra \simeq 7.5 \times 10^9$ the single-roll LSC splits into an inner-core and an outer-shell structure with different rotating frequencies and that the elliptical circulating roll also changes its orientation by 90° (Xia *et al.* 2003). If these features are indeed related to each other, then it means that a structural

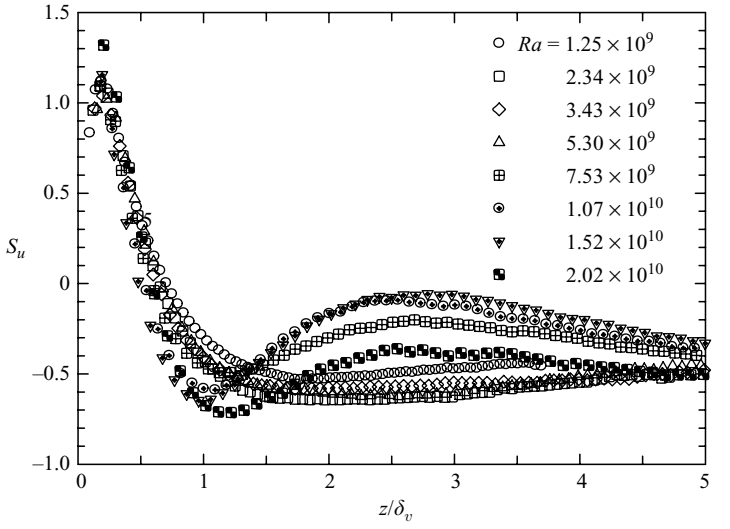

FIGURE 16. The evolution of the skewness S_u profiles with Ra.

change of the bulk flow field can influence the statistical properties of the velocity field in the boundary layer.

3.6. *Scaling of the profiles of the temperature and velocity fluctuations in the mixing zone*

An issue of considerable interest concerns the properties of the profiles of the temperature and velocity fluctuations. The scalings of these fluctuations with distance from the boundary are intimately related to heat transfer from the plates and various models make very different predictions for the related scaling behaviour. In some of the models, the r.m.s. value σ_T of the temperature and the r.m.s. value σ_w of the vertical velocity have been predicted to vary with the distance z from the horizontal wall as power laws, i.e. $\sigma_T \sim z^{\alpha}$ and $\sigma_w \sim z^{\beta}$. For example, in the classical theory for atmospheric boundary layers, Priestley (1959) has predicted the exponents $\alpha = -1/3$ and $\beta = 1/3$. In other models, logarithmic profiles have been suggested. As pointed out by Adrian (1996), the two versions of the mixing zone model by Castaing *et al.* (1989) entail different behaviours for σ_T and σ_w. In the first scenario (referred to as the λ-I theory by Adrian), velocity scales in the thermal boundary layer and convective central core were assumed to be the same and it was shown that σ_T follows a power law with $\alpha = -1/2$ while σ_w scales logarithmically with the distance (Adrian 1996). In the second scenario (the so-called λ-II theory), it was assumed that the characteristic temperature scales in the thermal boundary layer and in the central core are the same and it was shown that both σ_T and σ_w follow logarithmic laws.

Both the classical predictions of Priestley and the predictions of the mixing-zone theory have been tested experimentally in previous studies. But the results have been mixed. For example, Townsend (1959) found for convective motions of air in open-topped box heated from below that $\alpha = -0.6$; Belmonte *et al.* (1993, 1994) and Tilgner *et al.* (1993) measured temperature profiles in RB convection cells filled with water and pressurized SF_6 respectively and found that $\alpha = -0.8$ (water) and $\alpha = -0.72$ (SF_6). In an RB experiment using a rectangular cell filled with water, Fernandes & Adrian (2002) reported logarithmic profiles for both σ_T and σ_w. But

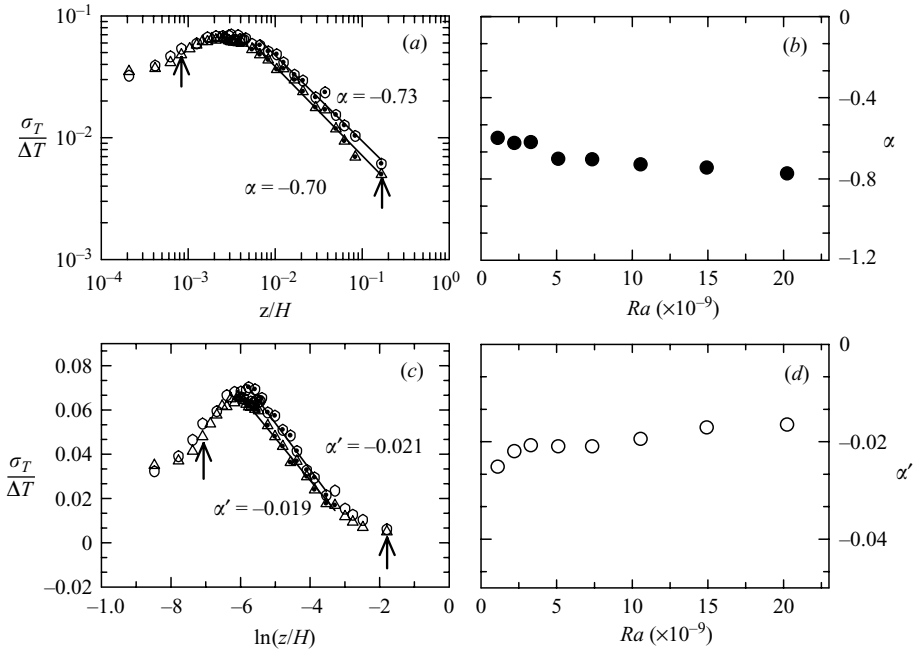

FIGURE 17. Left panels: Profiles of the normalized temperature r.m.s. $\sigma_T/\Delta T$ versus vertical distance in log-log (*a*) and semi-log (*c*) plots; circles: $Ra = 5.3\times10^9$; triangles: $Ra = 1.07\times10^{10}$. The arrow on the left indicates the position of the thermal boundary layer and the arrow on the right indicates the boundary between the mixing zone and the convective central core (for $Ra = 1.07 \times 10^{10}$). Right panels: (*b*) The Ra-dependent exponent α for the power-law profile and (*d*) the Ra-dependent slope α' for the logarithmic profile.

because the scatter of their data, their σ_T profiles could be fitted to a power law with exponent α between $-1/2$ to $-1/3$. Furthermore, the highest Ra reached in their experiment is only 2×10^9, which does not seem to be high enough (see discussion below). More recently, du Puits *et al.* (2007) conducted an RB convection experiment using air and found a power-law profile for σ_T and that $-0.30 > \alpha > -0.42$ which depends on both Ra and Γ. But this dependence on Γ is probably due to the fact that in their experiment Ra and Γ were changed simultaneously by varying the cell height. Thus, it is seen that even for the temperature r.m.s. for which most experiments found a power-law behaviour, no universal value for the exponent has emerged. For the velocity r.m.s. profiles, experimental results are more scarce.

With both the temperature and vertical velocity r.m.s. profiles measured in the present work, we are in a position to systematically examine their scaling properties with the vertical height from the horizontal plate and also their Ra-dependent behaviour. Before looking for the power-law or logarithmic behaviours, we should first bear in mind the regions in which these laws are predicted to hold. For example, Priestley (1959) suggested that the power-law behaviour for σ_T and σ_w should be present in a region sufficiently far away from the plate, i.e. outside the boundary layer. If it is outside the boundary layer but not in the convective core, this region should be in the so-called 'mixing zone' proposed by Castaing *et al.* (1989). So it is the profile properties in the mixing zone that we shall focus our attention on. We examine the temperature data first. Figures 17(*a, c*) plot the profiles of the normalized temperature r.m.s. $\sigma_T/\Delta T$ versus the normalized vertical distance z/H from the

bottom plate on both log-log (*a*) and semi-log (*c*) scales. For clarity, only data for two values of *Ra* are shown. In both plots the arrow on the left indicates the boundary between the thermal boundary layer and the mixing zone and the arrow on the right separates the mixing zone and the convective central core, the thermal boundary layer has been determined in § 3.1.

The mixing zone is determined based on the properties of the 'plus' and 'minus' temperature skewness profiles in a previous study (Zhou & Xia 2002). This result has been confirmed recently in a study of the geometrical and mixing properties of thermal plumes in which it was shown that the mixing zone can be quantitatively defined as the overlap region of the profile of the vertical vorticity fluctuations and profile of the mushroom-like thermal plumes and that the mixing zone is a region characterized by strong fluctuations of the vertical vorticity (Zhou, Sun & Xia 2007*a*). Figure 17(*b*, *d*) shows the *Ra*-dependence of the exponent α for the power-law profiles and the slope α' for the logarithmic profiles. The r.m.s. profiles in figure 17(*a, c*) show clearly that temperature fluctuations reach their maximum value just outside the thermal boundary layer and that a scaling range falls within the mixing zone. Figure 17 also shows that both the power-law and the logarithmic dependence can be fitted to the measured temperature r.m.s. profiles to some degree. Although the power-law fitting may be slightly favoured due to the fitting quality and the range of length scale over which it can be fitted, for the given experimental resolution we cannot definitively conclude which is a better choice. Also note that the exponent α for the power-law changes from -0.6 to -0.77 and the slope α' for the logarithmic profile also changes from -0.025 to -0.017. The variation of the power-law exponent, although not large but nonetheless beyond the experimental uncertainties, suggests a lack of universality for the profiles of different *Ra*. In this respect, our result is similar to that of du Puits *et al.* (2007) that α changes with *Ra*, although values of the exponent differ a lot in the two experiments and our result is definitely different from the classical value of $-1/3$ predicted by Priestley. On the other hand, our exponent values are comparable to those found by Tilgner *et al.* (1993) in water (-0.8) and in SF_6 (-0.72).

Figure 18 shows the results for the profiles of the normalized vertical velocity r.m.s. σ_w/U_{max} (note that one of these has been shown in figure 14 on a linear scale). The structure of the figure is similar to figure 17. Unlike in figure 17, here the arrow denotes the position of the viscous boundary layer. Because the velocity measurements were made only near the boundary layer region, the upper boundary of the mixing zone that separates it from the convective central core is not covered by the data. It is seen that here the fluctuations of the vertical velocity experience a local minimum at the boundary between the viscous boundary layer and the mixing zone. With regard to the scaling behaviour, the situation here is no less inconclusive than the temperature case. Both power-law and logarithmic fit appear to have comparable quality and both the power-law exponent β (between 0.25 and 0.67) and the slope β' (from 0.15 to 0.04) of the logarithmic profile vary a lot over the range of *Ra* spanned in the experiment. So here again, we cannot favour either the power-law profile or the logarithmic one. A possible reason is that the value of *Ra* reached in the present experiment is not high enough for σ_T and σ_w to exhibit a sufficiently wide scaling range so that different behaviour may be distinguished. One interesting feature however, is that at large *Ra* the exponent β appears to be approaching an asymptotic value which is smaller than Priestley's classical value of 1/3. As our last data point is already at the largest achievable *Ra* of the present apparatus, this trend can only be verified by future experiments.

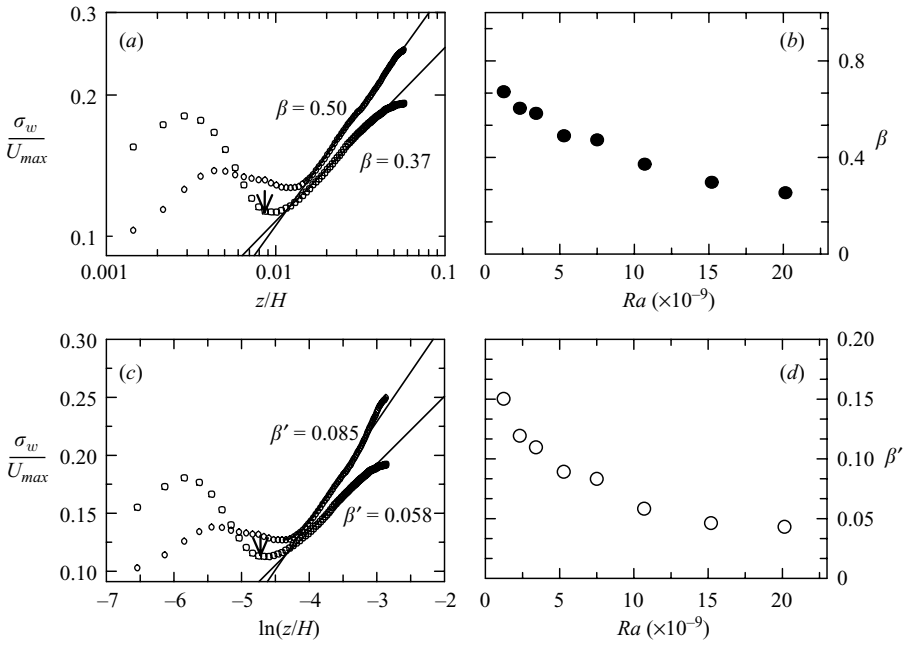

FIGURE 18. Left panels: Profiles of the vertical velocity r.m.s. σ_w/U_{max} versus normalized vertical distance in log-log (*a*) and semi-log (*c*) plots; circles: $Ra = 5.3 \times 10^9$; squares: $Ra = 1.07 \times 10^{10}$. The arrow indicates the position of the viscous boundary layer δ_υ (for $Ra = 1.07 \times 10^{10}$). Right panels: (*b*) The Ra-dependent exponent β for the power-law profile and (*d*) the Ra-dependent slope β' for the logarithmic profile.

3.7. *Shear stress distribution in the boundary layer*

From the Reynolds number dependence of the boundary layer thickness we have found that boundary layer is laminar and that it satisfies the Blasius condition in the present range of Rayleigh number. To determine when the laminar boundary layer will change to a turbulent one we examine the relative contributions of the viscous and Reynolds stresses to the total shear stress in the boundary layers. The viscous stress measures momentum transfer in the boundary layer due to viscosity, whereas the Reynolds stress measures momentum transfer due to turbulent velocity fluctuations. In other words, if the boundary layer is dominated by the viscous shear stress, it is laminar. On the other hand, if the Reynolds shear stress dominates, then the boundary layer is turbulent. The viscous shear stress is defined as $\mu \mathrm{d}U/\mathrm{d}z$, where μ is the dynamic viscosity. As μ has a strong dependence on the distance z from the plate because of the steep temperature gradient in the boundary layer, we write the viscous shear stress $\tau_v = \mu(z)\mathrm{d}U(z)/\mathrm{d}z$, where $\mu(z)$ and $U(z)$ are z-dependent viscosity and velocity. The Reynolds (or turbulent) shear stress is defined as $\tau_R = -\rho(z)\langle u'(z)w'(z)\rangle$, where $\rho(z)$ is the z-dependent density, and u' and w' are the fluctuations of the x and z components of the velocity respectively. The total shear stress is then $\tau(z) = \tau_v + \tau_R$.

Figure 19 plots the profiles of the viscous shear stress and Reynolds stress components for $Ra = 5.3 \times 10^9$. We can clearly see that the Reynolds stress τ_R is near zero and the viscous shear stress τ_v is maximum at the plate because of the large velocity gradient $\mathrm{d}U/\mathrm{d}z$. So the total stress $\tau(z)$ at the wall τ_w $(= \tau(0))$ comes almost entirely from the contribution of the viscous shear stress. As one moves away from the plate, the velocity gradient becomes smaller and the viscous shear stress

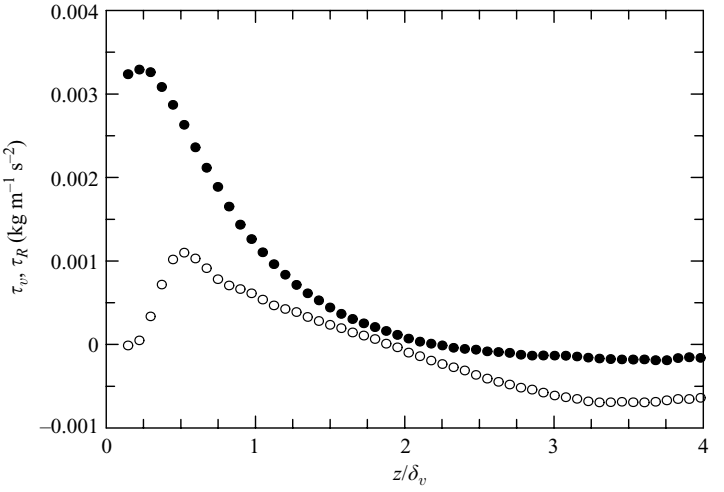

FIGURE 19. Viscous stress τ_v (solid circles) and the Reynolds stress τ_R (open circles) as functions of the normalized distance from the plate ($Ra = 5.3 \times 10^9$).

τ_v decreases to a negligible value. The Reynolds shear stress τ_R, on the other hand, increases from zero to a positive value with increasing z, and τ_R reaches a maximum at $z \simeq 0.5\delta_v$, then decreases with further increase in z. The Reynolds shear stress τ_R is around zero when z is around $2\delta_v$, it becomes negative in the outer flow with effect of thermal plumes and large-scale flow. It is also seen clearly from the figure that $\tau_R < \tau_v$ within and around the boundary layer. This suggests that the momentum transfer in the boundary layer is dominated by viscous diffusion rather than turbulent fluctuations, which is consistent with the laminar boundary layer found above. We may also compare the relative weights of the viscous stress and the Reynolds stress by examining their respective ratios to the total shear stress, i.e. τ_v/τ and τ_R/τ. Figure 20 plots on a semi-log scale the Ra-dependence of τ_v/τ and τ_R/τ measured at the viscous boundary layer thickness δ_v. The figure shows that as Ra increases the contribution of the viscous stress decreases while that of the Reynolds stress increases. But at the highest value of Ra reached in the experiment the viscous stress is still larger than the Reynolds stress. On the other hand, the figure suggests that a crossover will occur around $Ra = 3 \times 10^{10}$ if the present result is extrapolated. This would imply that around this Ra half of the momentum transfer in the boundary layer will be made by viscous diffusion and the other half by turbulent fluctuations, and that above this Ra turbulent fluctuations will become the dominant mechanism for momentum transfer. Thus $Ra \simeq 3 \times 10^{10}$ may be regarded as the onset value for the boundary layer to become turbulent. We stress, however, that at this Ra the boundary layer still cannot be considered as turbulent.

3.8. *Scaling properties of boundary layer quantities*

The universal laws of boundary layers in systems such as pipe flows have been well-studied theoretically, numerically and experimentally (Eggels *et al.* 1994; Schlichting & Gersten 2000; Shang 2002). Assuming that the boundary layer in thermal convection has similar characteristics as in classical shear flows, Shraiman & Siggia (1990) and Siggia (1994) derived the Ra dependence of Nu and Re as $Nu \sim Ra^{2/7}$ and $Re \sim Ra^{3/7}[2.5\ln(Re) + 6.0]$. They assumed that the velocity in the boundary layer has

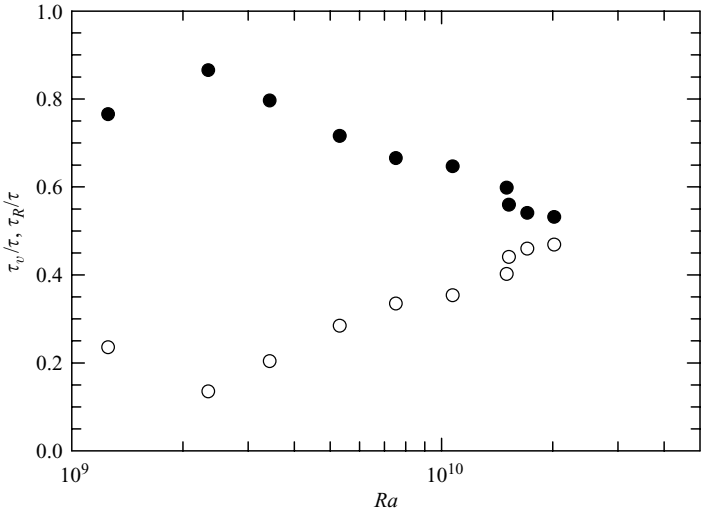

FIGURE 20. Ra-dependence of the viscous stress (solid circles) and the Reynolds stress (open circles) normalized by the total shear stress at the position of the viscous boundary layer.

a logarithmic region, which leads to a logarithmic correction to the *Ra*-dependence of *Re*. However, Tilgner *et al.* (1993) found that the distance between the edge of the viscous sublayer and the point of maximum velocity is too small to determine whether an intrinsically logarithmic profile follows the linear region. Xin *et al.* (1996), Xin & Xia (1997) and Qiu & Xia (1998*b*) also found no signs of logarithmic profiles in their direct velocity measurements over a wide range of *Ra*. As most of the previous studies were focused on mean velocity measurements with very limited resolution, the wall properties cannot be determined. So it is not possible to compare the obtained boundary layer properties with those from classical shear flows.

With the measured near-wall high-resolution velocity field, we are now in a position to check the wall properties in turbulent thermal convection. We first consider the scalings of four basic wall quantities with both *Ra* and *Re*. These are the wall shear stress $\tau_w = \tau(z)|_{z=0}$, which is just the viscous shear stress at the wall (plate) as the Reynolds shear stress vanishes there; the friction velocity $u_\tau = (\tau_w/\rho_o)^{1/2}$; the viscous sublayer (or the wall thickness) $\delta_w = \nu_o/u_\tau$; and the skin-friction coefficient $c_f = \tau_w/(\rho_o U_{max}^2)$. Here $\rho_o \equiv \rho(z)|_{z=0}$ and $\nu_o \equiv \nu(z)|_{z=0}$. Figure 21 shows the scaling of these quantities with *Ra*. Reasonably good scalings are seen for all these quantities, except perhaps c_f. We are not aware of any theoretical prediction for the *Ra*-scaling of these quantities in turbulent thermal convection. So we examine the scaling of these quantities with the Reynolds number, for which comparison may be made with other types of flows. These are shown in figure 22, where *Re* is based on the maximum velocity U_{max} defined in § 3.3. It is seen that the wall shear stress τ_w scales as $Re^{1.55}$, the friction velocity u_τ scales as $Re^{0.8}$, and the viscous sublayer δ_w scales as $Re^{-0.91}$. For a laminar boundary layer over a flat plate, the theoretically predicted 'classical' exponents for these quantities are 3/2, 3/4, and -1 (apart from a logarithmic correction), respectively (Schlichting & Gersten 2000). Thus the experimental exponents are close to, but nevertheless different from, the classical ones. The differences may be a reflection of the fact that in the present case a thermal boundary layer with intermittent emission of plumes is nested within the viscous layer. If this is the case, then the small differences imply that the presence of a

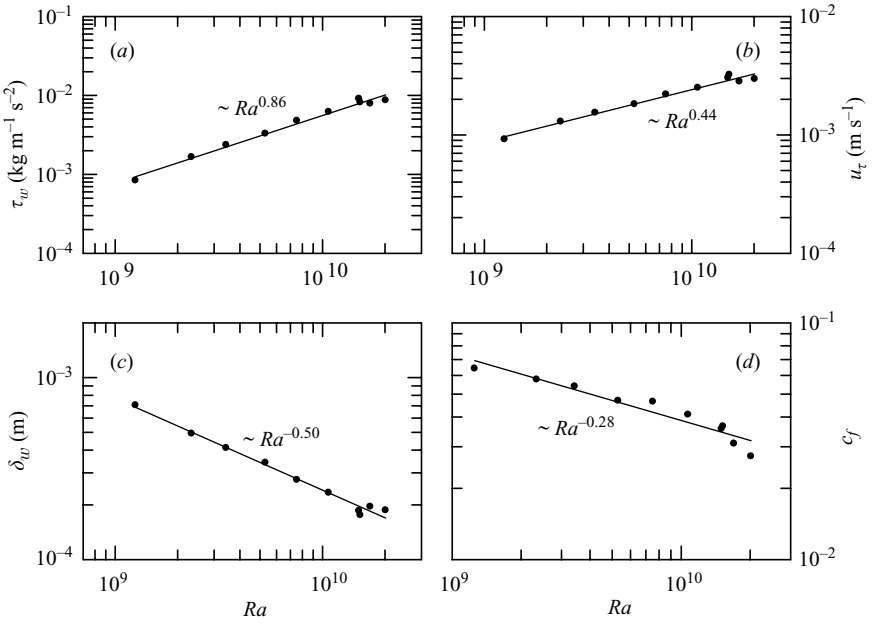

FIGURE 21. The Ra-dependence of (a) the wall shear stress τ_w, (b) the friction velocity u_τ, (c) the wall thickness (viscous sublayer) δ_w, and (d) the friction coefficient c_f.

thermal boundary layer does not significantly modify the time-averaged quantities of the classical laminar layer in the present range of Ra and Pr.

For the friction coefficient c_f, the scaling exponent of -0.34 differs significantly from the theoretical value of $-1/2$. But with the poor quality of the power-law scaling, it is difficult to attach much importance to this discrepancy. In a numerical study of thermal convection in a cylindrical cell with Pr matching that of helium gas, Verzicco & Camussi (2003) found that c_f computed over all solid surfaces shows a scaling consistent with $Re^{-1/2}$, while c_f computed only over the horizontal plates shows a change in slope at Re around a few thousand. In the present case, the measured c_f is also seen to change slope at $Re \sim 5000$, although the Re range in each part is rather narrow. Whether this feature in the two cases is related requires further investigation. The overall conclusion from the above is that, despite the presence of a thermal boundary layer with sharp temperature gradient, the (time-averaged) near-wall quantities within the viscous sublayer in turbulent thermal convection do not differ significantly from the classical case of a laminar layer over a flat plate.

To further compare the present system with classical boundary layers, we examine velocity profiles in terms of the wall units. Figure 23 shows the normalized mean horizontal velocity profiles for four different values of Ra in a semi-log plot, here $U^+ = U(z)/u_\tau$ and $z^+ = z/\delta_w$. The two vertical dashed lines indicate the positions of the thermal boundary layer δ_{th}, which varies from $z^+ = 2$ to 4 from high to low values of Ra. We can clearly see that a viscous sublayer obeying $U^+ = z^+$ exists within the velocity boundary layer, despite the presence of the thermal boundary layer. However, a departure from the linear relation can be observed near the edge of the viscous sublayer, i.e. $z^+ = 5$. This deviation may be caused by the emission of thermal plumes, since the region is just outside the thermal boundary layer as indicated in the figure. From the figure it is also evident that a logarithmic region is

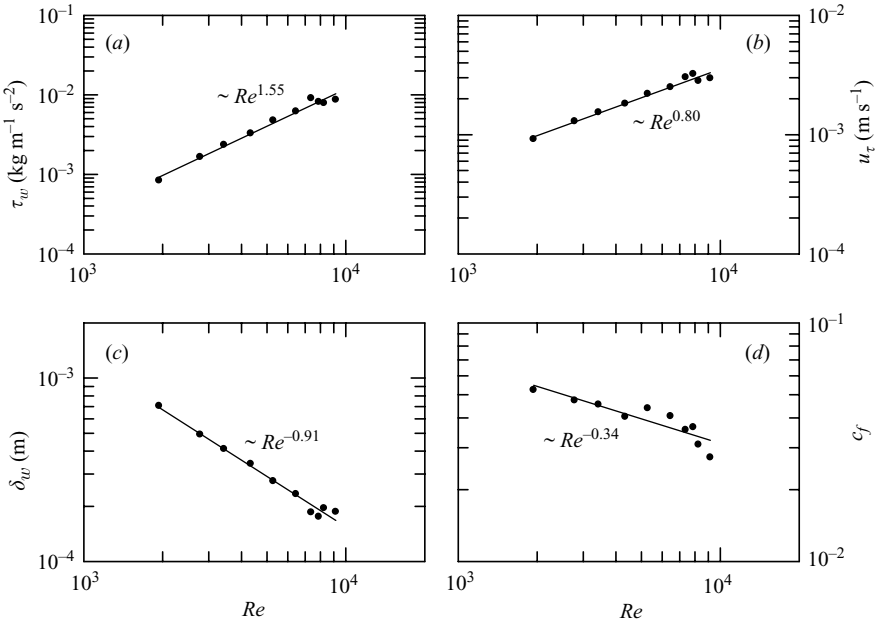

FIGURE 22. The Re-dependences of (a) the wall shear stress τ_w, (b) the friction velocity u_τ, (c) the wall thickness (viscous sublayer) δ_w, and (d) the friction coefficient c_f.

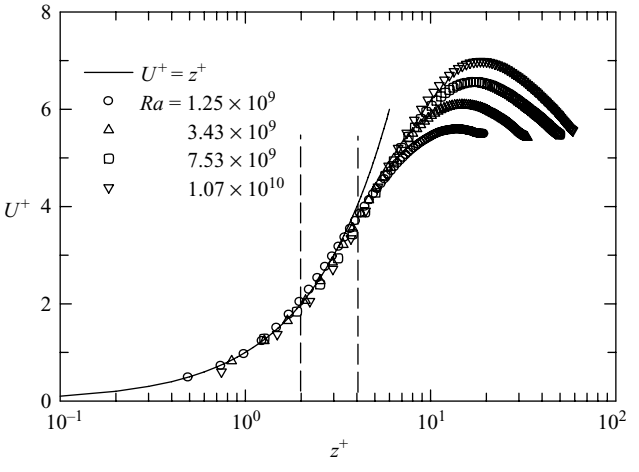

FIGURE 23. Measured horizontal velocity profiles normalized by wall units for four different Ra. The two vertical dashed lines indicate the positions of the thermal boundary layer δ_{th}, which varies from $z^+ = 2$ to 4 with increasing Ra.

absent from the measured velocity profiles. The lack of a log-law region is another confirmation that the boundary layer is not turbulent in the present range of Ra and Pr. Another feature of the profiles is that the velocity decays quickly after reaching its maximum value around several tens of z^+. This is related to the fact that the mean flow in the central region of a closed convection cell is zero (Qiu & Tong 2001; Xia *et al.* 2003). Thus the properties of the flow field in the bulk have a strong influence on its properties in boundary layer. This is very different from open systems like channel

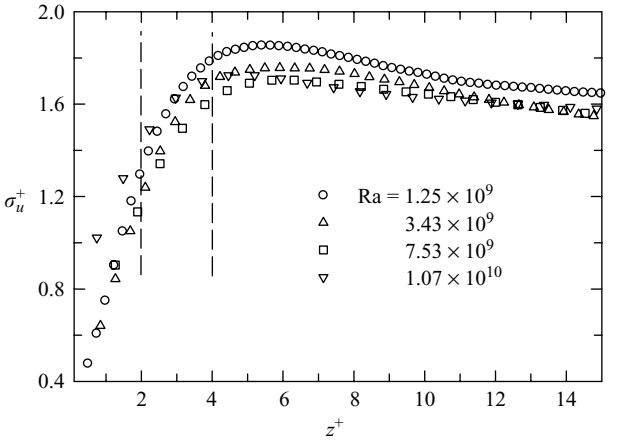

FIGURE 24. Measured profiles of the horizontal velocity r.m.s. normalized by wall units for four different *Ra*. The two vertical dashed lines indicate the positions of the thermal boundary layer δ_{th}, which varies from $z^+ = 2$ to 4 with increasing *Ra*.

or pipe flows in which the velocity is maximum over an extended region in the central part of the system. Note that the profile for the highest *Ra* in figure 23 appears to exhibit a logarithmic region between $z^+ = 4$ and 10. However, as this region is rather narrow and appears only for the highest *Ra*, we refrain from making this a conclusive observation. It is known that for classic shear flows the logarithmic regime appears for $z^+ > 30$, so if the above observation of a possible logarithmic regime is indeed confirmed in future studies it would imply that in thermal convective flows the log-layer is shifted significantly toward the wall.

The root-mean-square velocities for four different *Ra*, normalized by friction velocities, i.e. $\sigma_u^+ = \sigma_u(z)/u_\tau$, are presented in figure 24. Again, the vertical dashed lines indicate the range of the thermal boundary layers for the various *Ra*. The peak of the horizontal velocity fluctuation is seen to be around $z^+ \sim 5$. The closeness to the wall of the maximum velocity fluctuations is another difference between turbulent thermal convection and wall-bounded shear flow. For example, for pipe flows the peak position of r.m.s. velocity fluctuations is around $z^+ \sim 12$ (Eggels *et al.* 1994; Shang 2002). In the present case the position $z^+ \sim 5$ is just outside the thermal boundary layer. Therefore the large velocity fluctuations may be caused by the intermittent emission of thermal plumes. Comparing figure 24 with figure 15, which also plots r.m.s. profiles with different normalizations, it is seen that σ_u^{max} and δ_σ are the relevant quantities for these profiles. This is perhaps another difference between the boundary layers in turbulent thermal convection and classical shear flows.

3.9. *Possible implications of the present results*

The overall conclusion one can draw from the results presented in this paper is that, despite the existence of many differences, especially in the statistical quantities, in a time-averaged sense, the viscous boundary layer remains laminar in the present range of the *Ra* and *Pr*, and that the intermittent emissions of coherent structures (the thermal plumes) from the boundary layer do not modify its properties in any significant way from those of classical shear flows. One may therefore ask what would happen at much higher values of *Ra*. We have seen in § 3.6 that a crossover between the viscous stress and the Reynolds stress at the position of the viscous boundary

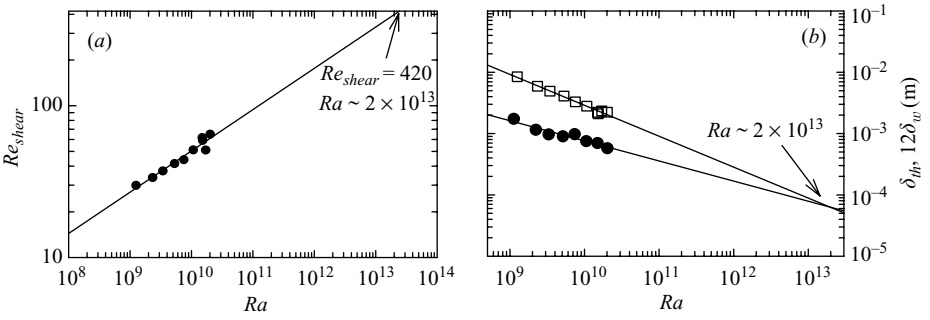

FIGURE 25. (*a*) *Ra*-dependence of the shear Reynolds number Re_{shear}. The extrapolation of experimental data indicates that the boundary layer becomes turbulent ($Re_{shear} = 420$) at $Ra \simeq 2 \times 10^{13}$. (*b*) *Ra*-dependence of the measured thermal boundary layer thickness δ_{th} (solid circles) and $12\delta_w$ (open squares) (δ_w is the viscous sublayer). The extrapolations of experimental data suggests that the two length scale would cross at $Ra \simeq 2 \times 10^{13}$, indicating turbulent fluctuations penetrating the thermal boundary at this *Ra*.

layer will occur around $Ra = 3 \times 10^{10}$, suggesting this may be the onset *Ra* for the boundary layer to become turbulent. At this *Ra* turbulent fluctuations only reach the viscous boundary layer while the thermal boundary layer that nests inside the viscous one is still laminar, which means that heat transfer across that layer is still by conduction. As our boundary layer is very similar to those in traditional shear flows, we may use knowledge from studying the classical boundary layers to examine when our boundary layer will become 'fully turbulent', or when a new regime of heat transfer may emerge.

The first criterion involves the so-called (boundary-layer-thickness-based) shear Reynolds number, which is defined as $Re_{shear} = U\delta_v/\nu$, where U is the time-averaged velocity at δ_v. The critical value for the instability of the boundary layer (i.e. the boundary layer becomes turbulent) is $Re_{shear} = 420$ (see, for example, Landau & Lifshitz 1987). Using the measured values of δ_v and U the *Ra*-dependence of Re_{shear} can be obtained, which is plotted in figure 25(*a*). The result shows that for the values of *Ra* reached in the present experiment Re_{shear} is well below the critical value, again consistent with a laminar boundary layer. From an extrapolation of the current result we see that a turbulent boundary layer is expected to occur at $Ra \simeq 2 \times 10^{13}$.

The second criterion for a fully turbulent boundary layer uses the empirical result that in turbulent boundary layers the viscous shear stress and the Reynolds (or turbulent) shear stress are equal at a distance of $z^+ = 12$ from the wall, i.e. at $z = 12\delta_w$ (see, for example, Niemela & Sreenivasan 2003), where δ_w is the viscous sublayer thickness. When this distance becomes smaller than the thermal layer δ_{th}, turbulent fluctuations will have penetrated the thermal layer and the heat transport inside δ_{th} will then be controlled by turbulence rather than conduction. In figure 25(*b*) we plot both δ_{th} (solid circles) and $12\delta_w$ (open squares) *vs* *Ra*, which again shows that the thermal layer is far from turbulent for the present *Ra*. Again the extrapolations of the experimental data suggest that for $Ra \geqslant 2 \times 10^{13}$ turbulent fluctuations will penetrate the thermal layer. Note that the second extrapolation involves temperature measurements that are independent of the velocity measurements, so the two extrapolations are really independent of each other. Therefore, it is interesting that the extrapolations based on two different criteria both indicate that for $Ra > 2 \times 10^{13}$ a new regime may emerge. This is the so-called ultimate regime in turbulent thermal

convection predicted by Kraichnan, in which heat transport is expected to be influenced strongly by boundary layer turbulence (Kraichnan 1962). It should be noted that, by extrapolating two measured length scales, the thermal boundary layer thickness and the length scale associated with the position of the maximum cutoff frequency of temperature signal, Belmonte *et al.* (1994) found that the two scales should cross near $Ra \gtrsim 10^{14}$, which is close to the present result. In a turbulent helium gas convection experiment, Chavanne *et al.* (1997) observed a transition of the scaling behaviour of Nu with Ra for $Ra \gtrsim 10^{11}$, which they interpreted as the signature for transition to the Kraichnan regime. However, such a transition was not observed in other similar experiments (Niemela *et al.* 2000; Niemela & Sreenivasan 2003). This further suggests that global heat transport measurements alone may not be sufficient to resolve the issue on the existence of the Kraichnan regime and that direct boundary layer measurements at very high Ra should shed some light on this problem.

4. Summary and conclusions

In this paper we have presented results from high-resolution measurements of various quantities of the velocity boundary layer in turbulent thermal convection. These are obtained using the particle image velocimetry (PIV) technique in a rectangular cell with the Rayleigh number Ra varying from 10^9 to 10^{10} and the Prandtl number Pr fixed at 4.3, using water as the convecting fluid. Temperature profiles are also measured near the bottom plate of the convection cell for the same values of Ra and Pr. Although these measurements are primarily for obtaining the profiles of the temperature-dependent fluid properties, the thermal boundary layer thickness is also determined.

From the velocity measurement two length scales are obtained, which are the velocity (or viscous) boundary layer thickness δ_v base on the mean horizontal velocity profile and the r.m.s. velocity boundary layer thickness δ_σ based on the r.m.s. horizontal velocity profile. It is found that the scaling of δ_v with the Reynolds number satisfies the classical Blasius-type laminar boundary layer for the present range of Ra and Pr, i.e. $\delta_v \sim Re^{-0.50}$; and that δ_σ scales with Re as $\delta_\sigma \sim Re^{-0.72}$, for which we are not aware of any theoretical predictions. It is also found that, within the experimental resolution, the thermal boundary layer thickness δ_{th} and the r.m.s. velocity boundary layer thickness δ_σ approximately coincide. By comparing the relative strengths of the viscous shear stress and the Reynolds shear stress at the boundary layer, we conclude that the velocity boundary layer remains laminar for the highest Rayleigh number reached in the present experiment ($\sim 2 \times 10^{10}$). The fact that the viscous boundary layer remains laminar, in a time-averaged sense, despite the existence of the intermittent emission of thermal plumes, can also be seen from the direct visualization of the velocity field near the boundary as shown in figure 4. Two independent extrapolations of the present result, one based on velocity measurements and the other on velocity and temperature measurements, both indicate that the viscous boundary layer will become turbulent at $Ra \sim 2 \times 10^{13}$.

With regard to the scaling of the temperature (σ_T) and velocity (σ_w) r.m.s. profiles, it is found that σ_T can be described by either a power law or logarithmic law of the vertical distance from the horizontal plate, i.e. $\sigma_T(z)/\Delta T \sim (z/H)^\alpha$ and $\sigma_T(z)/\Delta T \sim \alpha' \ln(z/H)$, with the power-law behaviour being more favourable. The exponent α is found to depend on Ra and varies from -0.6 to -0.77, which is much larger than the classical value of $-1/3$ predicted by Priestley. In the same region, the measured

profiles $\sigma_w(z)$ of the r.m.s. vertical velocity exhibit a much smaller scaling range and are also consistent with either a power law ($\sigma_w(z)/U_{max} \sim (z/H)^{\beta}$) or a logarithmic ($\sigma_w(z)/U_{max} \sim \beta' ln(z/H)$) behaviour. Similar to the temperature case, the exponent β and the slope β' also vary with Ra, but with much stronger Ra-dependence.

It is also found that, similar to traditional shear flows, there exists a classical viscous sublayer in turbulent thermal convection despite the fact that a thermal boundary layer nests within the viscous boundary layer in this system. On the other hand, velocity profiles normalized by wall units exhibit no obvious logarithmic region, which is probably a result of the very limited distance between the edge of the viscous sublayer and the position of the maximum velocity. Compared to traditional shear flows, the peak positions of r.m.s. profiles are found to be closer to the plate (at $z^+ \simeq 5$). The Reynolds number dependence of several wall quantities are also measured directly. These are the wall shear stress $\tau_w \sim Re^{1.55}$, the viscous sublayer $\delta_w \sim Re^{-0.91}$, the friction velocity $u_\tau \sim Re^{0.80}$, and the skin-friction coefficient $c_f \sim Re^{-0.34}$. All of these scaling properties are very close to those predicted for classical Blasius-like laminar boundary layers, except that of c_f. These results suggest that the logarithmic correction in various scaling exponents is not obvious in the present system. Our overall conclusion is that the Blasius-like laminar boundary condition, in a time-averaged sense, is a good approximation for the velocity boundary layer in turbulent thermal convection for the present ranges of the Rayleigh number and the Prandtl number.

We have benefitted from stimulating conversations with many colleagues during the High Rayleigh Number Convection Workshops held in Leiden (2003) and Trieste (2006), respectively. In particular, we would like to thank B. Castaing, S. Grossmann, D. Lohse and K. R. Sreenivasan for helpful discussions. This work is supported by the Hong Kong Research Grants Council under Project Nos. CUHK 403705 and 403806.

REFERENCES

Adrian, R. J. 1991 Particle-imaging techniques for experimental fluid mechanics. *Annu. Rev. Fluid Mech.* **23**, 261–304.

Adrian, R. J. 1996 Variation of temperature and velocity fluctuations in turbulent thermal convection over horizontal surfaces. *Intl. J. Heat Mass Transfer* **39**, 2303–2310.

Ahlers, G. & Xu, X. 2001 Prandtl-number dependence of heat transport in turbulent Rayleigh–Bénard convection. *Phys. Rev. Lett.* **86**, 3320–3323.

Amati, G., Koal, K., Massaioli, F., Sreenivasan, K. R. & Verzicco, R. 2005 Turbulent thermal convection at high Rayleigh numbers for a Boussinesq fluid of constant Prandtl number. *Phys. Fluids* **17**, 121701.

Ashkenazi, S. & Steinberg, V. 1999 High Rayleigh number turbulent convection in a gas near the gas-liquid critical point. *Phys. Rev. Lett.* **83**, 3641–3644.

Belmonte, A., Tilgner, A. & Libchaber, A. 1993 Boundary layer length scales in thermal turbulence. *Phys. Rev. Lett.* **70**, 4067–4070.

Belmonte, A., Tilgner, A. & Libchaber, A. 1994 Temperature and velocity boundary layers in turbulent convection. *Phys. Rev.* E **50**, 269–279.

Breuer, M., Wessling, S., Schmalzl, J. & Hansen, U. 2004 Effect of inertia in Rayleigh–Bénard convection. *Phys. Rev.* E **69**, 026302.

Brown, E., Funfschilling, D. & Ahlers, G. 2007 Anomalous Reynolds-number scaling in turbulent Rayleigh–Bénard convection. *J. Statist. Mech.* P10005.

Brown, E., Nikolaenko, A. & Ahlers, G. 2005 Reorientation of the large-scale circulation in turbulent Rayleigh–Bénard convection. *Phys. Rev. Lett.* **95**, 084503.

Burr, U., Kinzelbach, W. & Tsinober, A. 2003 Is the turbulent wind in convective flows driven by fluctuations? *Phys. Fluids* **15**, 2313–2320.

Castaing, B., Gunaratne, G., Heslot, F., Kadanoff, L., Libchaber, A., Thomae, S., Wu, X.-Z., Zaleski, S. & Zanetti, G. 1989 Scaling of hard thermal turbulence in Rayleigh–Bénard turbulent convection. *J. Fluid Mech.* **204**, 1–30.

Chavanne, X., Chillà, F., Castaing, B., Hébral, B., Chabaud, B. & Chaussy, J. 1997 Observation of the ultimate regime in Rayleigh–Bénard convection. *Phys. Rev. Lett.* **79**, 3648–3651.

Chavanne, X., Chillà, F., Chabaud, B., Castaing, B. & Hébral, B. 2001 Turbulent Rayleigh–Bénard convection in gaseous and liquid He. *Phys. Fluids* **13**, 1300–1320.

Ching, E. S. C. 1997 Heat flux and shear rate in turbulent convection. *Phys. Rev.* E **55**, 1189–1192.

Ching, E. S. C. & Tam, W. S. 2006 Aspect-ratio dependence of heat transport by turbulent Rayleigh–Bénard convection. *J. Turbulence* **7(72)**, 1–10.

Cioni, S., Ciliberto, S. & Sommeria, J. 1997 Strongly turbulent Rayleigh–Bénard convection in mercury: comparison with results at moderate Prandtl number. *J. Fluid Mech.* **335**, 111–140.

Du, Y.-B. & Tong, P. 1998 Enhanced heat transport in turbulent convection over a rough surface. *Phys. Rev. Lett.* **81**, 987–990.

Dubrulle, B. 2001 Logarithmic corrections to scaling in turbulent thermal convection. *Eur. Phys. J.* B **21**, 295–304.

Eggels, J. G. M., Unger, F, Weiss, M. H., Westerweel, J., Adrian, R. J., Friendrich, R. & Nieuwstadt, F. T. M. 1994 Fully developed turbulent pipe flow: a comparison between direct numerical simulation and experiment. *J. Fluid Mech.* **268**, 175–209.

Eidelman, A., Elperin, T., Kleeorin, N., Markovich, A. & Rogachevskii, I. 2006 Hysteresis phenomenon in turbulent convection. *Exps. Fluids* **40**, 723–732.

Fernandes R. L. J. & Adrian R. J. 2002 Scaling of velocity and temperature fluctuations in turbulent thermal convection. *Expl Thermal Fluid Sci.* **26**, 355–360.

Funfschilling, D., Brown, E., Nikolaenko, A. & Ahlers, G. 2005 Heat transport by turbulent Rayleigh–Bénard convection in cylindrical samples with aspect ratio one and larger. *J. Fluid Mech.* **536**, 145–154.

Glazier, J. A., Segawa, T., Naert, A. & Sano, M. 1999 Evidence against 'ultrahard' thermal turbulence at very high Rayleigh numbers. *Nature* **398**, 307–310.

Grossmann, S. & Lohse, D. 2000 Scaling in thermal convection: A unifying theory. *J. Fluid Mech.* **407**, 27–56.

Grossmann, S. & Lohse, D. 2001 Thermal convection for large Prandtl numbers. *Phys. Rev. Lett.* **86**, 3316–3319.

Grossmann, S. & Lohse, D. 2003 On geometry effects in Rayleigh–Bénard convection. *J. Fluid Mech.* **486**, 105–114.

Grossmann, S. & Lohse, D. 2004 Fluctuations in turbulent Rayleigh–Bénard convection: The role of plumes. *Phys. Fluids* **16**, 4462–4472.

Haramina, T. & Tilgner A. 2004 Coherent structures in boundary layers of Rayleigh–Bénard convection. *Phys. Rev.* E **69**, 056306.

Kadanoff, L. P. 2001 Turbulent heat flow: Structures and scaling. *Phys. Today* **54**, 34–39.

Kenjereš, S. & Hanjalić, K. 2002 Numerical insight into flow structure in ultraturbulent thermal convection. *Phys. Rev.* E **66**, 036307.

Kerr, R. M. 1996 Rayleigh number scaling in numerical convection. *J. Fluid Mech.* **310**, 139–179.

Kerr, R. M. & Herring, J. R. 2000 Prandtl number dependence of Nusselt number in direct numerical simulations. *J. Fluid Mech.* **419**, 325–344.

Kraichnan, R. H. 1962 Turbulent thermal convection at arbitrary Prandtl number. *Phys. Fluids* **5**, 1374–1389.

Krishnamurti, R. & Howard, L. N. 1981 Large-scale flow generation in turbulent convection. *Proc. Natl. Acad. Sci. USA* **78**, 1981–1985.

Lam, S., Shang, X.-D., Zhou, S.-Q. & Xia, K.-Q. 2002 Prandtl number dependence of the viscous boundary layer and the Reynolds numbers in Rayleigh–Bénard convection. *Phys. Rev.* E **65**, 066306.

Landau, L. D. & Lifshitz, E. M. 1987 *Fluid Mechanics.* Pergamon.

Lui, S.-L. & Xia, K.-Q. 1998 Spatial structure of the thermal boundary layer in turbulent convection. *Phys. Rev.* E **57**, 5494–5503.

Naert, A., Segawa, T. & Sano, M. 1997 High-Reynolds-number thermal turbulence in mercury. *Phys. Rev.* E **56**, R1302–1305.

Niemela, J. J., Skrbek, L., Sreenivasan, K. R. & Donnely, R. J. 2000 Turbulent convection at very high Rayleigh numbers. *Nature* **404**, 837–840.

Niemela, J. J. & Sreenivasan, K. R. 2003 Confined turbulent convection. *J. Fluid Mech.* **481**, 355–384.

Niemela, J. J. & Sreenivasan, K. R. 2006 Turbulent convection at high Rayleigh numbers and aspect ratio 4. *J. Fluid Mech.* **557**, 411–422 .

Nikolaenko, A., Brown, E., Funfschilling, D. & Ahlers, G. 2005 Heat transport by turbulent Rayleigh–Bénard convection in cylindrical cells with aspect ratio one and less. *J. Fluid Mech.* **523**, 251–260.

Priestley, C. H. B. 1959 *Turbulent Transfer in the Lower Atmosphere*. University of Chicago Press.

Puits, R. Du, Resagk, C., Tilgner, A., Busse, F. H. & Thess, A. 2007 Structure of thermal boundary layers in turbulent Rayleigh–Bénard convection. *J. Fluid Mech.* **572**, 231–254.

Qiu, X.-L. & Tong, P. 2001 Large-scale velocity structures in turbulent thermal convection. *Phys. Rev.* E **64**, 036304.

Qiu, X.-L. & Xia, K.-Q. 1998*a* Viscous boundary layers at the sidewall of a convection cell. *Phys. Rev.* E **58**, 486–491.

Qiu, X.-L. & Xia, K.-Q. 1998*b* Spatial structure of the viscous boundary layer in turbulent convection. *Phys. Rev.* E **58**, 5816–5820.

Schlichting, H. & Gersten, K. 2000 *Bounday Layer Theory*. Springer.

Shang, X.-D. 2002 Statistics, scaling and structures in fluid turbulence: Case studies for thermal convection and pipe flow. PhD thesis. The Chinese University of Hong Kong.

Shang, X.-D., Qiu, X.-L., Tong, P. & Xia, K.-Q. 2003 Measured local heat transport in turbulent Rayleigh–Bénard convection. *Phys. Rev. Lett.* **90**, 074501.

Shraiman, B. I. & Siggia, E. D. 1990 Heat transport in high-Rayleigh-number convection. *Phys. Rev.* A **42**, 3650–3653.

Siggia, E.D. 1994 High Rayleigh number convection. *Annu. Rev. Fluid Mech.* **26**, 137–168.

Sun, C., Ren, L.-Y., Song, H. & Xia, K.-Q. 2005*a* Heat transport by turbulent Rayleigh–Bénard convection in 1 m diameter cylindrical cells of widely varying aspect ratio *J. Fluid Mech.* **542**, 165–174.

Sun, C., Xi, H.-D. & Xia, K.-Q. 2005*b* Azimuthal symmetry, flow dynamics, and heat flux in turbulent thermal convection in a cylinder with aspect ratio one-half. *Phys. Rev. Lett.* **95**, 074502.

Sun, C. & Xia, K.-Q. 2005 Scaling of the Reynolds number in turbulent thermal convection. *Phys. Rev.* E **72**, 067302.

Sun, C., Xia, K.-Q. & Tong, P. 2005*c* Three-dimensional flow structures and dynamics of turbulent thermal convection in a cylindrical cell. *Phys. Rev.* E **72**, 026302.

Sun, C., Zhou, Q. & Xia, K.-Q. 2006 Cascades of velocity and temperature fluctuations in buoyancy-driven thermal turbulence. *Phys. Rev. Lett.* **97**, 144504.

Takeshita, T., Segawa T., Glazier, J. A. & Sano, M. 1996 Thermal turbulence in mercury. *Phys. Rev. Lett.* **76**, 1465–1468.

Thomas, D. B. & Townsend, A. A. 1957 Turbulent convection over a heated horizontal surface. *J. Fluid Mech.* **2**, 473–492.

Tilgner, A., Belmonte, A. & Libchaber A. 1993 Temperature and velocity profiles of turbulent convection in water. *Phys. Rev.* E **47**, R2253–R2256.

Townsend, A. A. 1959 Temperature fluctuations over an heated surface. *J. Fluid Mech.* **5**, 209–241.

Verzicco, R. & Camussi, R. 2003 Numerical experiments on strongly turbulent thermal convection in a slender cylindrical cell. *J. Fluid Mech.* **477**, 19–49.

Wang, J. & Xia, K.-Q. 2003 Spatial variations of the mean and statistical quantities in the thermal boundary layers of turbulent convection. *Eur. Phys. J.* B **32**, 127–136.

Xi, H.-D., Zhou, Q. & Xia, K.-Q 2006 Azimuthal motion of the mean wind in turbulent thermal convection. *Phys. Rev.* E **73**, 056312.

Xia, K.-Q. 2007 Two clocks for a single engine in turbulent convection. *J. Statist. Mech.* N11001.

Xia, K.-Q., Lam, S. & Zhou, S.-Q. 2002 Heat-flux measurement in high-Prandtl-number turbulent Rayleigh–Bénard convection. *Phys. Rev. Lett.* **88**, 064501.

Xia, K.-Q. & Qiu, X.-L. 1999 Turbulent convection with "disconnected" top and bottom boundary layers. *Europhy. Lett.* **46**, 171–176.

Xia, K.-Q., Sun, C. & Zhou, S.-Q. 2003 Particle image velocimetry measurement of the velocity field in turbulent thermal convection. *Phys. Rev.* E **68**, 066303.

Xia, K.-Q., Xin, Y.-B. & Tong, P. 1995 Dual-beam incoherent cross-correlation spectroscopy. *J. Opt. Soc. Am.* A **12**, 1571–1578.

Xia, K.-Q. & Zhou, S.-Q. 2000 Temperature power spectra and the viscous boundary layer in thermal turbulence: the role of Prandtl number. *Physica* A **288**, 308–314 (2000).

Xin, Y.-B. & Xia, K.-Q. 1997 Boundary layer length scales in convective turbulence. *Phys. Rev.* E **56**, 3010–3015.

Xin, Y.-B., Xia, K.-Q. & Tong, P. 1996 Measured velocity boundary layers in turbulent convection. *Phys. Rev. Lett.* **77**, 1266–1269.

Yaws C. L. 1999 *Chemical Properties Handbook*. McGraw-Hill.

Zhou, Q., Sun, C. & Xia, K.-Q. 2007*a* Morphological evolution of thermal plumes in turbulent Rayleigh–Bénard convection. *Phys. Rev. Lett.* **98**, 074501.

Zhou, S.-Q., Sun, C. & Xia, K.-Q. 2007*b* Measured oscillations of the velocity and temperature fields in turbulent Rayleigh–Bénard convection in a rectangular cell. *Phys. Rev. E* **76**, 036301.

Zhou, Q., Sun, C. & Xia, K.-Q. 2008 Experimental investigation of homogeneity, isotropy, and circulation of the velocity field in buoyancy-driven turbulence. *J. Fluid Mech.* **598**, 361–372.

Zhou, S.-Q. & Xia, K.-Q. 2001 Spatially correlated temperature fluctuations in turbulent convection. *Phys. Rev.* E **63**, 046308.

Zhou, S.-Q. & Xia, K.-Q. 2002 Plume statistics in thermal turbulence: Mixing of an active scalar. *Phys. Rev. Lett.* **89**, 184502.

Zocchi, G., Moses, E. & Libchaber, A. 1990 Coherent structures in turbulent convection, an experimental study. *Physica* A **166**, 387–407.